Applied Catalysis B: Environmental 210 (2017) 352–367

Contents lists available at ScienceDirect

Applied Catalysis B: Environmental

journal homepage: www.elsevier.com/locate/apcatb

# Enhancement of photocatalytic performance with the use of noble-metal-decorated $TiO_2$ nanocrystals as highly active catalysts for aerobic oxidation under visible-light irradiation

Yu Chen, Yannan Wang, Weizun Li, Qian Yang, Qidong Hou, Lianghuan Wei, Le Liu, Fang Huang, Meiting Ju *

*College of Environmental Science and Engineering, Nankai University, Tianjin 300071, China*

ARTICLE INFO

*Article history:*
Received 8 November 2016
Received in revised form 22 March 2017
Accepted 31 March 2017
Available online 2 April 2017

*Keywords:*
Noble metal nanoparticles
Photocatalytic selective oxidation
Irradiation wavelength
Light intensity
Reaction temperature

ABSTRACT

The use of noble metals loaded on semiconductor supports, through the absorption of visible light by metal nanoparticles, has opened new avenues for the improvement of catalytic performance under light irradiation. In this study, a series of different coinage metals such as gold, silver, platinum, and palladium loaded on $TiO_2$ were prepared by photo-deposition and characterized by transmission electron microscopy, X-ray diffraction, Brunauer–Emmett–Teller analysis, UV–vis diffuse reflectance spectroscopy, photoluminescence emission, and X-ray photoelectron spectroscopy. The photocatalytic activity of M–$TiO_2$ (M = Au, Ag, Pt, and Pd) samples was evaluated by the selective oxidation of benzyl alcohol under visible-light irradiation. In addition, the relationship between the light intensity, light wavelength, temperature of the reaction, and photocatalytic efficiency was investigated; the photocatalytic efficiency increased directly by increasing the light intensity or reaction temperature or by adjusting the irradiation wavelength in the most appropriate range. Particularly, $Pt_2$–$TiO_2$, with a Pt nanoparticle size ~2 nm, created an Schottky barrier, so as to promote the electron transfer from platinum to titanium, which in turn promotes the aerobic oxidation of benzyl alcohol with an apparent quantum yield of 5.58% (at 400 nm). The mechanism of the oxidation process of benzyl alcohol over $Pt_2$–$TiO_2$ is also presented. In addition, platinum and palladium nanoparticles exhibited an even more profound improvement in catalytic performance at a high operating temperature (80 °C); these catalysts can be used as photo-thermocatalyst, which can more efficiently drive chemical conversion by coupling light and heat energy sources.



## 1. Introduction

The oxidation of primary and secondary alcohols to the corresponding carbonyl compounds is a basic and useful organic reaction, owing to diverse applications of carbonyl compounds as important building blocks for the fragrances and drug industries [1–7]. Typically, oxidation reactions use stoichiometric oxidizing agents such as chromate ($Cr^{6+}$) or permanganate ($Mn^{7+}$); however, these processes are hazardous, delivering considerable amounts of toxic waste [8]. Thus, the exploration of a cost-efficient and environmentally friendly method for the selective oxidation of aromatic alcohols to the corresponding carbonyl continues to attract significant interest.

Chemical transformation driven by photocatalytic reactions under mild conditions has been proposed as an attractive, environmentally benign method for organic synthesis. Several types of substrates such as alcohols, amines, hydrocarbons, and sulfides were successfully oxidized at atmospheric pressure and room temperature [9–23]. Enhancement of the efficiency of these synthetic reactions via light irradiation, particularly with solar energy, which is a reproducible, abundant, and "green" energy source, under mild conditions would be a significant achievement. Nevertheless, poor visible-light harvesting and low quantum efficiencies under visible-light irradiation, which is the main component of sunlight irradiation, are some of the typical drawbacks hindering the practical applications of photocatalytic processes. To circumvent these drawbacks, one of the promising strategies for improving visible-light activity of photocatalyst is photosensitization with coinage metal nanoparticles (gold, silver, and platinum) via their visible-light absorption [24–32]. Very recently,

* Corresponding author.
*E-mail address:* jumeit@nankai.edu.cn (M. Ju).

http://dx.doi.org/10.1016/j.apcatb.2017.03.077
0926-3373/

noble metal/semiconductor system has been recognized as photo-induced carrier generation and injection; noble metal nanoparticles supported on semiconductors absorb visible light and excite energetic electrons via the intra- or inter-band transition of the 6 sp or 5 d band, then these hot electrons inject into the semiconductor conduction band over the interface between the metal and semiconductor, promoting the reduction of molecular oxygen adsorbed on the surface. In this process, molecular oxygen plays a key role in enhancing photocatalysis by serving as an electron scavenger, thus reducing the recombination of electrons and holes, as well as forming highly oxidative species, which are desirable for photocatalytic reactions.

So far, monometals such as Au, Pt, and Pd have been extensively investigated for the selective oxidation of aromatic alcohols [26,33–38]. Shiraishi et al. reported the use of P25 $TiO_2$-loaded Au particles for the aerobic oxidation of benzyl alcohol under visible-light irradiation ($\lambda > 450$ nm) and found that the location of Au NPs at the interface anatase/rutile $TiO_2$ is crucial for the transformation of electron from LSPR-excited Au NPs to $O_2$. In the plasmonic reaction, the charge separation is facilitated by the reduction of $O_2$ on the semiconductor surface, affording high yields of aldehyde or ketone products under visible-light irradiation [26]. Then, they reported that the use of anatase $TiO_2$-loaded Pt particles with a diameter in the range 3–4 nm for visible-light aerobic oxidation. The platinum atoms created a relatively low Schottky barrier at the Pt/anatase interface, facilitating transformation of photoelectrons and highly efficiently promoting the reaction [35]. Recently, Wang et al. reported the use of Pd decorated $TiO_2$ nanocrystals with mainly exposed (001) facets, exhibiting high activity for the selective photocatalytic oxidation of aromatic alcohols in an aqueous medium under UV light irradiation [39]. Despite the high activity of Au–P25, Pt–anatase, and Pd–$TiO_2$ for the selective photo-oxidation of alcohols, the effect of the factors such as light intensity, light wavelength, and reaction temperature on the photocatalytic activity over metal–semiconductor systems have been largely overlooked.

For complete understanding of the superior photocatalytic activity of noble-metal-modified titania under visible-light irradiation, a detailed comparative investigation is needed, taking account of light intensity, reaction temperature, and light wavelength. To the best of our knowledge, no such study has been reported so far. Therefore, herein, a series of different noble metals such as gold, silver, platinum, palladium, loaded on $TiO_2$ were prepared by a general one-step *in situ* photodeposition. The photocatalytic activities of M–$TiO_2$ (M = Au, Ag, Pt, and Pd) samples were evaluated by the photocatalytic selective oxidation of benzyl alcohol. With strict limitations of other influencing factors, direct correlation was observed between the light intensity, light wavelength, reaction temperature, and photocatalytic activity, which are of significance for designing a photocatalyst with improved performance. The photocatalytic mechanism of selective oxidation of benzyl alcohol over $Pt_2$-$TiO_2$ is also proposed. We hope that our study will provide useful information and promote further interest in the design and preparation of metallic nanoparticles loaded on semiconductors for target applications in solar energy conversion.

## 2. Experimental

### 2.1. Synthesis

#### 2.1.1. Synthesis of $TiO_2$ nanocrystals with hollow structure ($TiO_{2-H}$)

$TiO_{2-H}$ nanocrystals were prepared according to our previous study [16]. In a typical synthesis, 3.54 mL of acetic acid, 0.35 mL of water, and 4.372 mL of [Bmim][$BF_4$] were mixed in a Teflon beaker. Then, tetrabutyl titanate was added to the solution under magnetic stirring, resulting in a transparent solution. Finally, this homogeneous solution was placed in a microwave–solvothermal synthesis system (MDS-6, Sineo, Shanghai, China) and maintained at 200 °C for 4 h. The resulting powder was separated, centrifuged, washed with deionized water and anhydrous ethanol, and dried at 80 °C for 12 h.

#### 2.1.2. Photodeposition of noble metal

The noble metals were supported on hollow $TiO_2$ nanocrystal by a general one-step *in situ* photodeposition method. Here, the deposition of Au, Ag, Pt, and Pd was achieved using chloroauric acid ($HAuCl_4$, Sigma-Aldrich, 99.9%), silver nitrate ($AgNO_3$, Macklin, 99.8%), hexachloroplatinic(IV) acid ($H_2PtCl_6$, Macklin, 37.5% Pt), and palladium(II) chloride ($PdCl_2$, Sigma-Aldrich, 99.9%) as the precursors, respectively. Typically, for $Au_2$-$TiO_2$ (donated as 2 wt% of Au) sample, 4.125 mL $HAuCl_4$ (0.1 g/L) and $TiO_{2-H}$ (1 g) were dispersed in 40 mL methanol solution in a Pyrex glass reactor. Before the irradiation process, gaseous argon (Ar) was bubbled for 30 min to remove dissolved oxygen in the solution. Then, the mixture was subjected to UV light irradiation for 2 h using a high-pressure Mercury lamp (300 W). During the photodeposition process, the suspension gradually changed from white to auburn, indicating the reduction of Au precursors. The powder was collected by centrifugation and washed with anhydrous ethanol and water several times, and dried at 80 °C. Finally, the products were annealed in the air at 350 °C for 5 h before characterization and use.

### 2.2. Characterization

The crystal structure of the resulting materials was obtained by X-ray diffraction (PANalytical X'pert MRD) with a step size of 0.02° in the 2θ region 10–80°. UV–vis diffuse reflectance spectra of the samples were collected in the region from 300 to 800 nm using a Shimadzu 3600 UV–vis spectrophotometer. The morphologies of the photocatalysts were characterized by scanning electron microscopy (SEM, Hitachi S4800 microscope) and transmission electron microscopy (TEM, FEI Tecnai F20 microscope). The elemental composition of M–$TiO_2$ (M = Au, Ag, Pt, and Pd) samples was collected using energy-dispersive X-ray (EDX, Oxford-Instruments X-MaxN). The surface electronic states of the samples were analyzed by X-ray photoelectron spectroscopy (XPS, Thermo Fisher Scientific ESCALAB 250XI) under ultrahigh vacuum. The photoluminescence (PL) spectra were recorded using a Hitachi F-7000 fluorescence spectrophotometer. The excitation wavelength was 250 nm, the photoluminescence spectra recorded over the range of 270–800 nm, the scanning speed was 1200 nm/min, and the PMT voltage was 700 V. The width of excitation slit and emission slit were both 5.0 nm. The specific surface areas were calculated from the nitrogen adsorption/desorption isotherms collected at 77 K using a TriStar II 3020 adsorption analyzer. Electron spin resonance (ESR) signal of the radicals spin-trapped by 5,5-dimethyl-1-pyrroline-N-oxide (DMPO, supplied from Macklin) was recorded using a Magnet Tech MS400 spectrometer. Photocurrent and electrochemical impedance spectroscopy (EIS) measurements were carried out in a standard three electrode cell containing 0.5 mol $L^{-1}$ $Na_2SO_4$ aqueous solution with a platinum foil and a saturated calomel electrode as the counter electrode and the reference electrode, respectively, using a CHI 760D workstation (Shanghai, China). A 300 W Xe lamp with a 460 nm cutoff filter was chosen as a visible light source. All the electrochemical measurements were performed at room temperature.

### 2.3. Photocatalytic activity

The photocatalytic selective oxidation of alcohols was performed in a 15-mL a home-made reactor. Typically, a mixture of photocatalyst (10 mg) and 0.1 mmol of benzyl alcohol (reactant) was dissolved in trifluorotoluene (1.5 mL), and then injected into the reactor. The suspension was saturated with pure $O_2$ for 5 min and sealed with a rubber septum cap. Then, the bottle was ultrasonicated for 5 min to ensure that catalyst blended evenly in the solution. The suspension was photoirradiated under mag-

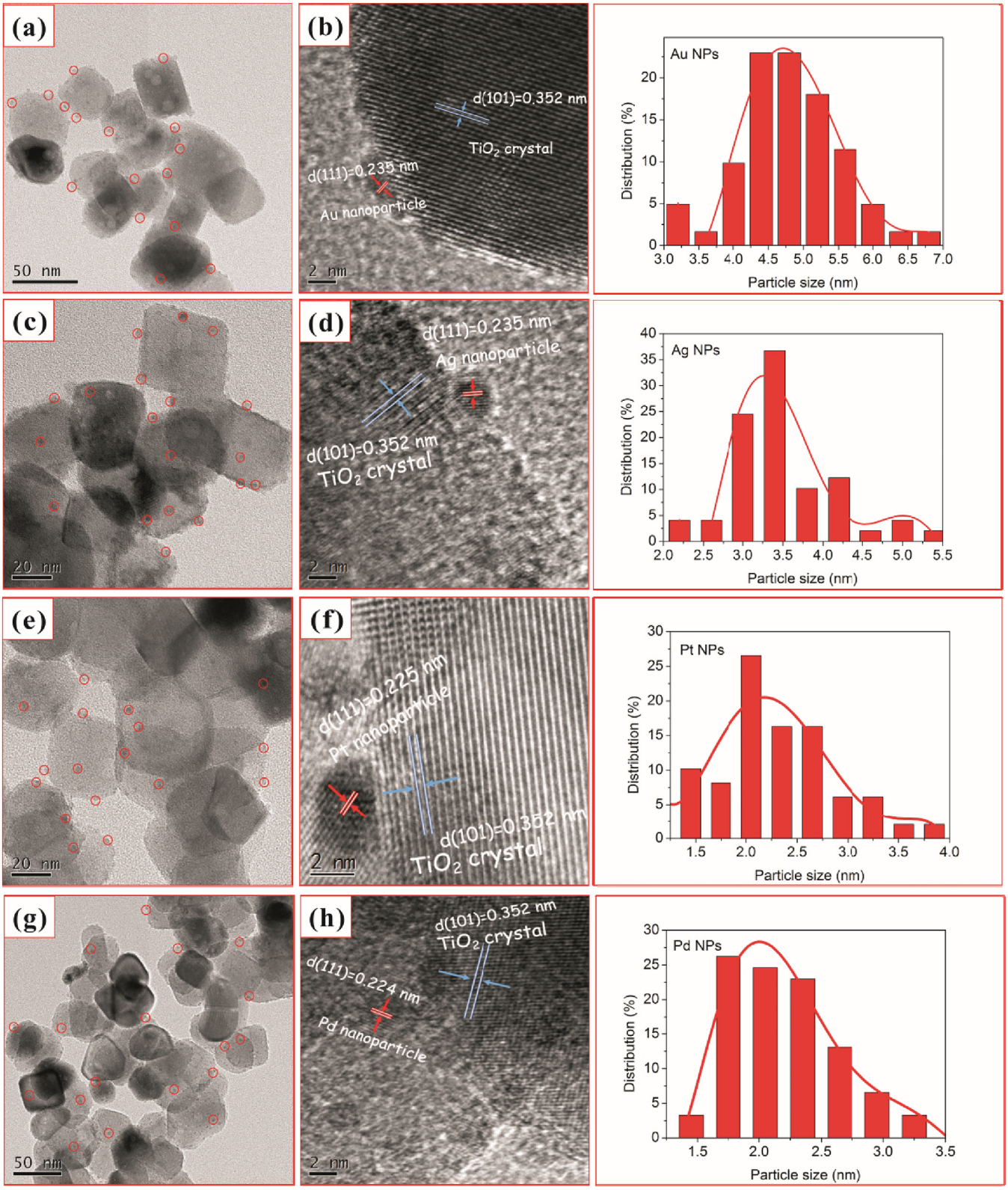


**Fig. 1.** TEM and HRTEM images of $TiO_{2\text{-}H}$ after loading with 2 wt% Au (a, b), Ag (c, d), Pt (e, f), and Pd (g, h) nanoparticles. Nanoparticle size distribution for the corresponding M–$TiO_2$ (M = Au, Ag, Pt, and Pd).

netic stirring using a 300 W xenon lamp (PLS-SXE 300, Beijing Perfectlight, Co. Ltd.) with a UV-cut filter to provide light with wavelengths λ > 460 nm. After the reaction, the catalyst was recovered by carefully washing with anhydrous ethanol and deionized water and dried in an oven at 80 °C overnight for the following cycling photoactivity test. The photocatalytic reaction temperature was controlled using a circular water system at room temperature. Different radical scavengers such as $AgNO_3$, ammonium oxalate (AO), *tert*-butyl alcohol (TBA), and benzoquinone (BQ) as the scavengers of photo-generated electrons, photo-generated holes, hydroxyl radical species, and superoxide radical species, respectively, were used in controlled photoactivity experiments. The experiment detail was similar to the above photocatalytic oxidation of benzyl alcohol except that radical scavengers (0.1 mmol) were added to the reaction system. The organic products were analyzed and identified by GC (Thermo Fisher TRACE 1310) and GC–MS (Thermo Fisher TRACE1310 and ISQ). The conversion of alcohol, yield, and selectivity of aldehyde were calculated by the following equations:

$$Conversion\,(\%) = \left[(C_0 - C_{alcohol})/C_0\right] \times 100$$

$$Yield\,(\%) = C_{aldehyde}/C_0 \times 100$$

$$Selectivity\,(\%) = \left[C_{aldehyde}/(C_0 - C_{alcohol})\right] \times 100$$

where $C_0$ is the initial amount of substrate alcohol before illumination; $C_{alcohol}$ is the amount of alcohol after illumination for 4 h; $C_{aldehyde}$ is the amount of the corresponding aldehyde after illumination the reaction.

## 3. Results and discussion

The morphology of the as-prepared samples was investigated by TEM, and the composition of Au, Ag, Pt, and Pd nanoparticles was analyzed by EDX spectroscopy. Fig. 1 shows the TEM and high-resolution transmission electron microscopy (HRTEM) images of $TiO_{2\text{-}H}$ loaded with 2 wt% of noble nanoparticles. The images clearly indicate the presence of spherical noble metal nanoparticles present on the surface of $TiO_2$ support material for different M–$TiO_2$ hybrid nanostructures. As illustrated by the red circles in Figs. 1(a, c, e, and g), Au, Ag, Pt, and Pd metal nanoparticles observed as dark dots were uniformly decorated on $TiO_2$ in each sample. The distribution of metal nanoparticles on $TiO_2$ support was quite even, and large conglomerates of NPs were not observed. Notably, the photoreduction of Pt(IV) or Pd(II) ions formed smaller nanoparticles (~2 nm) as compared to that of the solution consisting of the same amount of Au(III) or Ag(I) ions (nanoparticles ranged from 4 to 5 nm). The larger size of the Au nanoparticles, compared to the Pd and Pt nanoparticles, can be attributed to a weaker metal support interaction in the case of Au with $TiO_2$. This finding is consistent with that reported in a previous study with respect to the photoreduction of noble metal NPs on the surface of $TiO_2$ nanosheets with exposed {001} facets [40]. Regarding the $TiO_{2\text{-}H}$ support, the small 30–40 nm particles observed in the images (Figs. 1 and S1) can typically be identified as anatase, which is consistent with the XRD characterization. As shown in the HRTEM images in Fig. 1(b, d, f, and h), characteristic lattice fringes of 0.235, 0.235, 0.225, and 0.224 nm for Au, Ag, Pt, and Pd nanoparticles, respectively, were clearly observed and can be indexed as the (111) plane of face-centered cubic structures. The results obtained from EDX spectroscopy (Figs. S2 (a–d)) indicate that the composition of noble metals in M–$TiO_2$ (list in Table 1) are in good agreement with the nominal loading and near-surface region M:Ti ratios analyzed by the XPS analysis.

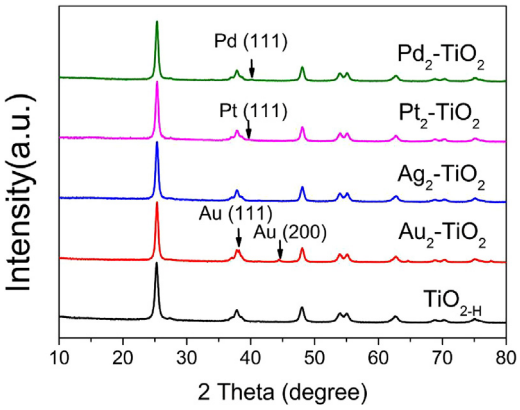


**Fig. 2.** XRD patterns of $TiO_{2\text{-}H}$ and 2 wt% M–$TiO_2$ catalysts (M = Au, Ag, Pt, and Pd).

The crystal structures of the $TiO_2$ nanocrystals were investigated by XRD. As shown in Figs. 2 and S3, the $TiO_2$ support material in all the samples was well crystallized by the microwave-assisted ionic liquid solvothermal treatment. Furthermore, $TiO_2$ nanocrystals synthesized using [Bmim][$BF_4$] ionic liquid exhibited a typical anatase structure without any impurity phases and is in good agreement with JCPDS card No. 21-1272. The characteristic diffraction peaks observed at 25°, 38°, 48°, 54°, 55°, 63°, 69°, 70°, and 75° were well indexed to the lattice planes of (101), (004), (200), (105), (211), (204), (116), (220), and (205) of anatase-phase $TiO_2$ nanostructures, respectively. Based on the linewidth analysis of the anatase (101) diffraction peak, the average crystal sizes of $TiO_{2\text{-}H}$ supports estimated by the Scherer equation were ~34.8 nm, in accordance with the suggested particle size of titania from the TEM results. Notably, typical diffraction peaks were not observed for Ag, Pt, or Pd in the diffraction patterns of the $Ag_2$–$TiO_2$, $Pt_2$–$TiO_2$, and $Pd_2$–$TiO_2$ photocatalysts, respectively, attributed to the even distribution and low

**Table 1**
Summarized physical,chemical and optical data for $TiO_{2\text{-}H}$ and the 2 wt% M–$TiO_2$ photocatalysts (M = Au, Ag, Pt or Pd).

| Sample | Metal content [a] (wt.%) | Mean metal particle size (nm)[b] | Band gap [b] (eV) | $S_{BET}$ [c] ($m^2$/g) | Pore size [d] (nm) | Pore volume [e] ($cm^3$/g) | Atom% by XPS | | | | | |
|---|---|---|---|---|---|---|---|---|---|---|---|---|
| | | | | | | | Ti | O | C [f] | M | O:Ti | M:Ti |
| $TiO_{2\text{-}H}$ | 0.00 | – | 3.08 | 57.77 | 12.14 | 0.36 | 24.03 | 56.24 | 19.73 | – | 2.34 | 0.000 |
| $Au_2$–$TiO_2$ | 2.07 | 4.81 | 3.03 | 59.15 | 11.44 | 0.31 | 24.08 | 56.23 | 18.98 | 0.70 | 2.33 | 0.029 |
| $Ag_2$–$TiO_2$ | 1.95 | 3.49 | 3.04 | 58.84 | 11.83 | 0.35 | 24.26 | 56.62 | 18.34 | 0.78 | 2.33 | 0.032 |
| $Pt_2$–$TiO_2$ | 2.11 | 2.19 | 3.05 | 56.99 | 10.82 | 0.29 | 24.38 | 56.35 | 18.50 | 0.77 | 2.31 | 0.031 |
| $Pd_2$–$TiO_2$ | 2.17 | 2.25 | 3.05 | 54.38 | 10.15 | 0.27 | 24.19 | 56.39 | 18.69 | 0.73 | 2.33 | 0.030 |

[a] Weight percentage of Au measured by EDS.
[b] Mean metal particle size statisticsed according to the TEM image.
[c] $S_{BET}$, BET surface areas calculated by the adsorption branch of the $N_2$ isotherm.
[d] $D_{BJH}$, pore diameter determined by BJH model.
[e] $V_t$, total pore volume.
[f] Adventitious hydrocarbons.

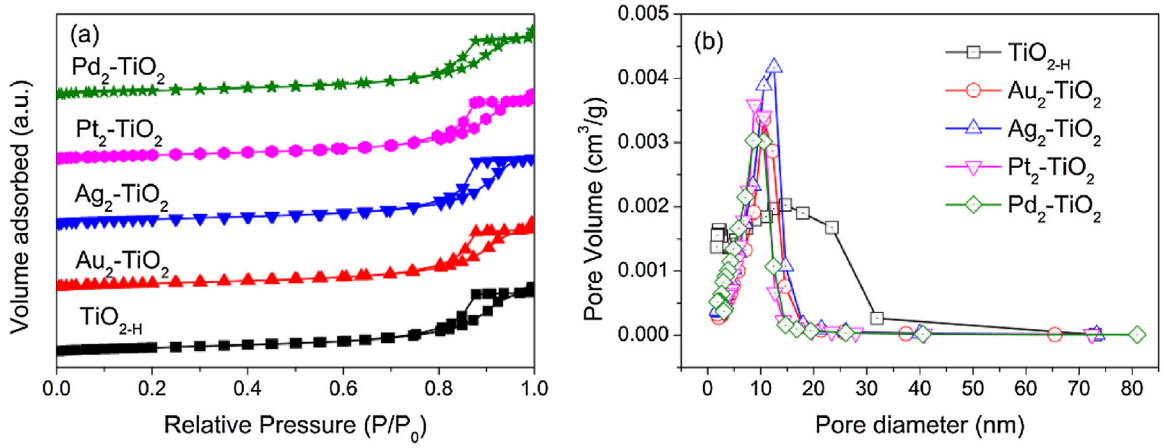


**Fig. 3.** (a) $N_2$ adsorption–desorption isotherms of $TiO_{2-H}$ and 2 wt% M–$TiO_2$ (M = Au, Ag, Pt, and Pd) nanocomposites, (b) corresponding pore size distribution.

weight loading of metal nanoparticles. For 2 wt% $Au_2$–$TiO_2$, some additional weak and broad peaks were observed and assigned to the fcc Au [41]. The most obvious of these peaks was the Au(200) reflection at 44°; in contrast, the Au(111) reflection observed at 38°, which was expected to be the most intense reflection for a statistically randomly distributed fcc Au powder, was obscured by those of anatase (103), (004), and (112). Owing to the small Pt and Pd nanoparticles sizes and the low nominal metal loadings, no diffraction peaks were observed for Pt or Pd in the diffraction patterns of the $Pt_2$–$TiO_2$ and $Pd_2$–$TiO_2$ photocatalysts, respectively.

For determining the surface area and pore size distribution of the obtained $TiO_{2-H}$ and 2 wt% M–$TiO_2$ (M = Au, Ag, Pt, and Pd) photocatalysts, BET characterization was conducted. Fig. 3 shows the nitrogen adsorption–desorption isotherms and the corresponding pore size distributions of supported materials of $TiO_{2-H}$ and the as-annealed M–$TiO_2$. All the samples exhibited a type IV nitrogen isotherm with an H3 hysteresis loop, which was confirmed by the corresponding pore size distribution, as shown in Fig. 3(b). For clearly observing the variations in the $TiO_{2-H}$ after the deposition of noble metals, the Brunauer–Emmett–Teller (BET) surface area, pore volume, and average pore size of the samples obtained from nitrogen adsorption–desorption isotherms are summarized in Table 1. All the samples clearly exhibited the similar surface area, whereas the pore volume and pore size decreased after the introduction of noble metal nanoparticles, attributed to the fact that noble metal nanoparticles loaded on the $TiO_2$ surface block support channels.

Fig. 4 shows the comparison between the optical response of noble-metal-loaded $TiO_2$ prepared by photoreduction and that of supported material $TiO_{2-H}$. All the photocatalysts exhibited strong absorption at <400 nm, attributed to the intrinsic absorption of the $TiO_2$ support. In contrast to the pure $TiO_2$, the samples deposited with Au NPs exhibited a significantly enhanced light absorption in the visible region, with a broad band peak located at ~570 nm, arising from the localized surface plasmon resonance (LSPR) effect of the gold nanoparticles. The $Ag_2$–$TiO_2$ catalysts exhibited a broad absorption feature centered at 550 nm and can be attributed to the LSPR effect of the supported silver nanoparticles [42]; this LSPR feature was responsible for the distinctive color of the $Au_2$–$TiO_2$ and $Ag_2$–$TiO_2$ photocatalysts and was consistent with the change in the color of the powders from white to purple and pink (the inset in Fig. 5). In contrast, the $Pt_2$–$TiO_2$ and $Pd_2$–$TiO_2$ catalysts exhibited intense absorption in the visible and NIR wavelengths and slightly increased as compared to that of $TiO_2$. This optical characteristic of Pd and Pt nanoparticles indicated that Pd and Pt nanoparticles do not exhibit localized surface plasmon absorption in the visible spectrum, attributed to a damping effect caused by d–d interband transitions [43,44]. As reported in previous studies [15,24,45–47], gold, silver, and platinum nanoparticles loaded on semiconductors such as $SrTiO_3$, $ZrO_2$, and $CeO_2$ with large absorption cross sections can absorb visible-light, trigger electrons intra- or interband transition via the 6sp or 5d band and produce hot electrons; these hot electrons are injected into the conduction band (CB) of the semiconductor over the interface between metal and semiconductor, facilitating the photo-generated carrier separation on the metal nanoparticles. In such a manner, metal nanoparticles can absorb

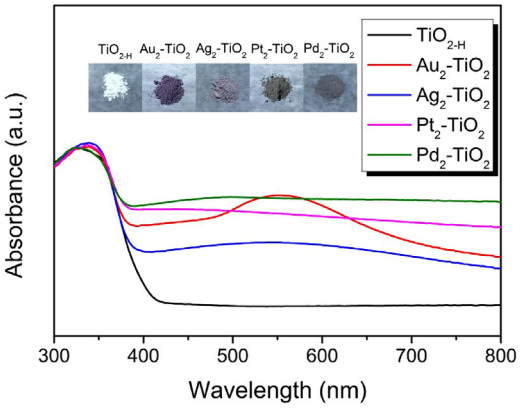


**Fig. 4.** UV–vis diffuse reflectance spectra (DRS) of $TiO_{2-H}$ and 2 wt% M–$TiO_2$ (M = Au, Ag, Pt, and Pd). The inset shows a digital photograph of the five samples.

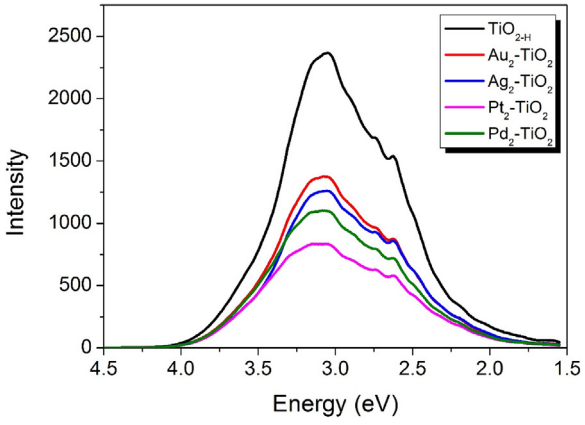


**Fig. 5.** Photoluminescence spectra of $TiO_{2-H}$ and 2 wt% M–$TiO_2$ (M = Au, Ag, Pt, and Pd).

visible-light and transfer solar energy to neighboring semiconductors or molecular complexes to drive chemical reactions.

The photoluminescence (PL) emission of the samples was also measured for understanding the behavior of light-generated electrons and holes in our samples, because PL emission results from the recombination of free carriers. Fig. 5 shows the PL spectra of M–$TiO_2$ (M = Au, Ag, Pt, and Pd) and $TiO_{2-H}$ samples at the wavelengths ranging from 270 to 800 nm (4.59 eV–1.55 eV) with light excitation at 250 nm. The shapes of the emission spectra of the different samples were similar. The emission peaks were centered at 400 nm (3.10 eV); these peaks are primarily attributed to direct transitions ($X_{1b} \rightarrow X_{1a}$, 3.45 eV and $X_{1b} \rightarrow X_{2b}$, 3.59 eV) and phonon-assisted indirect transitions ($X_{1b} \rightarrow \Gamma_3$, 3.19 eV, $\Gamma_{1b} \rightarrow X_{2b}$, 3.05 eV, and $\Gamma_{1b} \rightarrow X_{1a}$, 2.91 eV) of the anatase $TiO_2$ support [48,49]. In contrast, some weaker features were observed at the energies of 2.80, 2.70, 2.56, and 2.34 eV, attributed to oxygen vacancies and defects on the $TiO_2$ support [30]. The PL emission results suggested that the deposition of noble metals on $TiO_2$ strongly attenuates the PL signal of $TiO_2$, with the extent of attenuation following the order Pt > Pd > Au > Ag. The PL intensity versus $TiO_{2-H}$ decreased by 42%, 47%, 54%, and 65% for $Ag_2$–$TiO_2$, $Au_2$–$TiO_2$, $Pd_2$–$TiO_2$, and $Pt_2$–$TiO_2$, respectively. A lower PL intensity is generally indicative of a lower recombination rate of light generated charge carriers. Thus, this observation indicates that the charge-separation efficiency follows the order: $Pt_2$–$TiO_2$ > $Pd_2$–$TiO_2$ > $Au_2$–$TiO_2$ > $Ag_2$–$TiO_2$ > $TiO_{2-H}$. Therefore, it is concluded that the noble metal can effectively reduce the pair recombination of electrons and holes and increase the number of charge carriers ($h^+$ or $e^-$) available for photoreactions on the $TiO_2$ surfaces [50].

For identifying the effects of the surface electronic and states surface elemental composition of 2 wt% M–$TiO_2$ (M = Au, Ag, Pt, and Pd) and $TiO_{2-H}$ photocatalysts on their photocatalytic properties, the XPS characterization of Au, Ag, Pt, Pd, O, and Ti elements was performed, and survey scans were recorded, as shown in Figs. 6 and S5, respectively. Fig. 6a and b shows the XPS signature of the Au 4f doublet ($4f_{7/2}$ and $4f_{5/2}$) peaks and Ag 3d doublet ($3d_{5/2}$ and $3d_{3/2}$) for the Au and Ag nanoparticles supported on $TiO_2$, respectively. The Au 4f and Ag 3d doublet peaks were relatively narrow and symmetrical, indicating that gold and silver nanoparticles only exist in one chemical state. Au $4f_{7/2}$ and Au $4f_{5/2}$ peaks were observed at 83.9 and 87.6 eV, respectively, which were in agreement with the peaks characteristic for the metallic Au state. The XP spectrum of $Ag_2$–$TiO_2$ exhibited a symmetric Ag 3d signal at 368.3 eV (Ag $3d_{5/2}$) and 374.3 eV (Ag $3d_{3/2}$), corresponding to the binding energy of metallic $Ag^0$ (Fig. 6b). According to previous studies, a shift of 1.0 eV towards low binding energy was observed in the Au 4f and Ag 3d XPS spectra of $Au_2$–$TiO_2$ and $Ag_2$–$TiO_2$ as compared to that of bulk metallic gold and silver [51,52]; this negative binding energy shift is generally caused by a strong interaction between the gold, silver and $TiO_2$, in which electrons are transferred from the support material to the noble metal nanoparticles. As compared to the Au 4f and Ag 3d XPS signals, the Pd 3d and Pt 4f XPS peaks were rather broad and asymmetrical, indicating the existence of multiple chemical states of metals for palladium and platinum nanoparticles supported on $TiO_2$. As shown in Fig. 6c, the Pt $4f_{7/2}$ and $4f_{5/2}$ peaks decomposed into two components observed at 70.2/73.4 and 71.2/74.5 eV, corresponding to the metallic $Pt^0$ and $Pt^{2+}$ (PtO), respectively [53]. Similarly, the Pd $3d_{5/2}$ and $3d_{3/2}$ peaks can be decomposed into metallic $Pd^0$ and $Pd^{2+}$ (PdO) located at

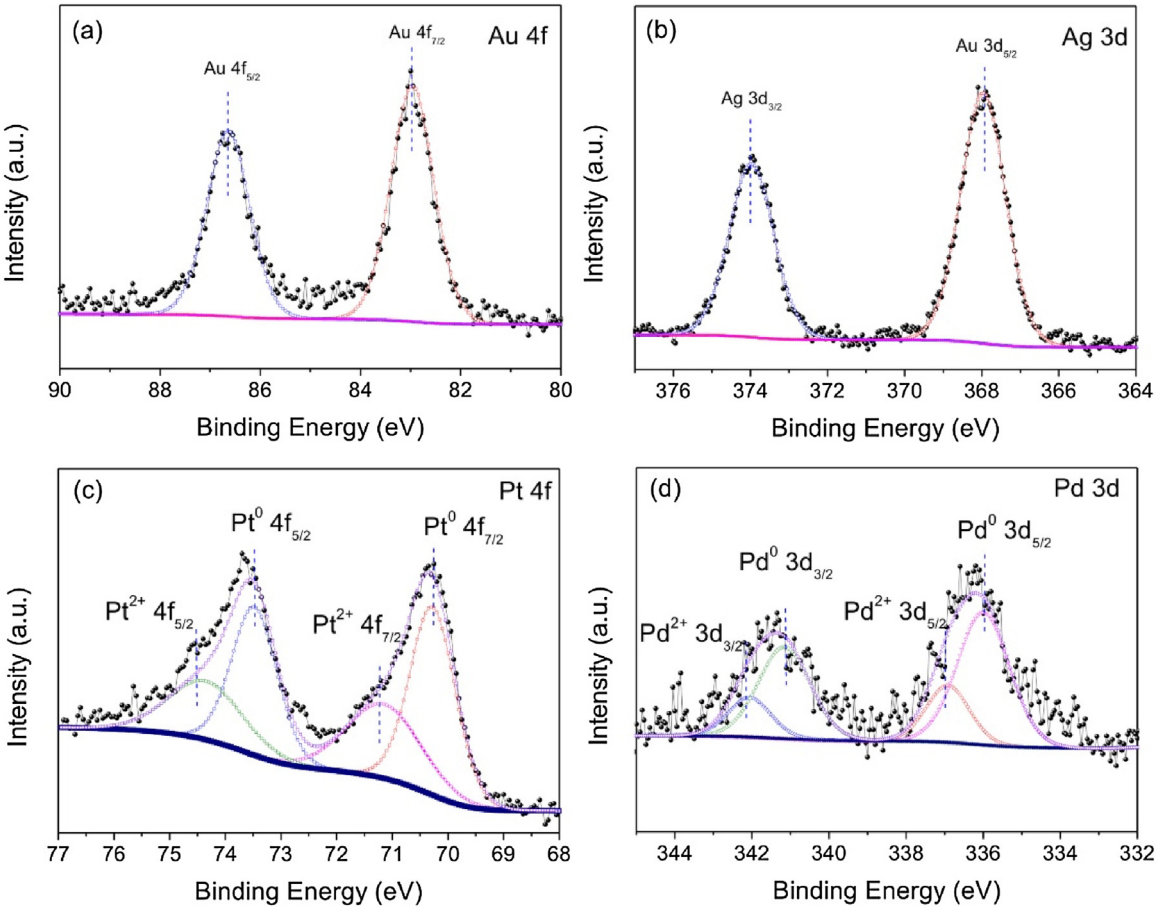


**Fig. 6.** Fine XP spectra of (a) Au 4f, (b) Ag 3d, (c) Pt 4f, and (d) Pd 3d obtained from 2 wt% M–$TiO_2$ (M = Au, Ag, Pt, and Pd).

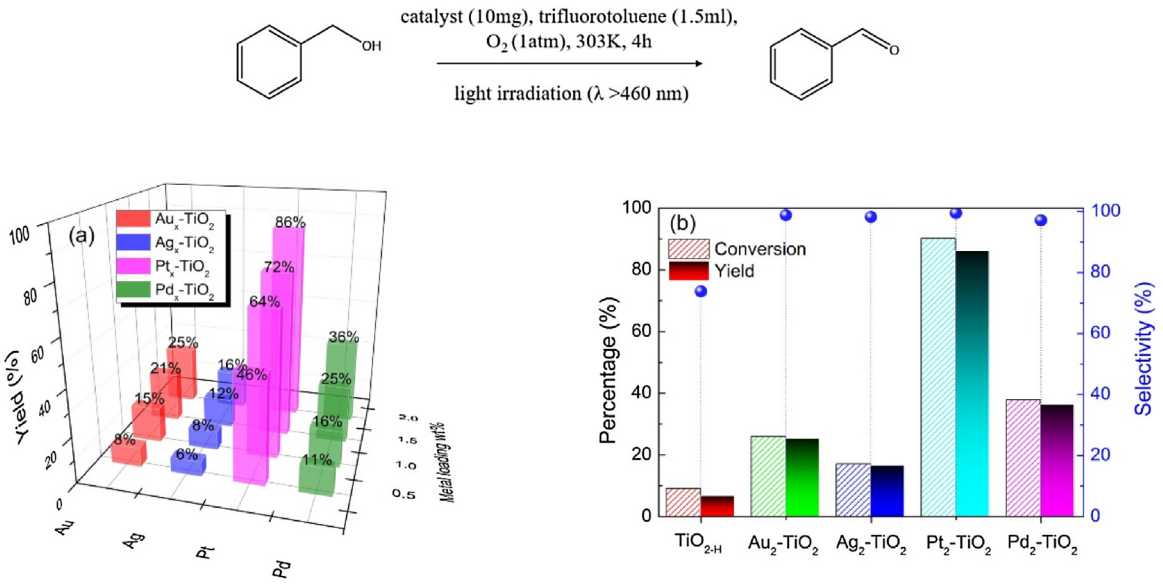


**Fig. 7.** (a) Yield of benzaldehyde formed during the oxidation of benzyl alcohol under visible-light irradiation (λ > 460 nm) over different amount (0.5–2 wt%) of metal-loaded M–$TiO_2$ (M = Au, Ag, Pt, and Pd). (b) Conversion, yield, and selectivity for the photo-oxidation of benzyl alcohol to benzaldehyde over $TiO_{2-H}$ and 2 wt% M–$TiO_2$ (M = Au, Ag, Pt, and Pd). Reaction conditions: catalyst (10 mg), benzyl alcohol (0.1 mmol), solvent trifluorotoluene (1.5 mL), $O_2$ atmosphere, reaction time 4 h, and temperature 30 °C, light source (300 W xenon lamp with λ > 460 nm).

336.0/341.2 and 337.0/342.2 eV, respectively. The relative scale of the two components indicates that $Pt_2$–$TiO_2$ and $Pd_2$–$TiO_2$ metals are mainly in the zero-valence state (i.e., $Pd^0$ and $Pt^0$), and their surfaces are partially oxidized. Furthermore, the Ti 2p signals (Fig. S5 (c)) were highly symmetric, and shoulders were not observed on the low energy side of the Ti 2p signals. As for the O 1 s spectrum, two characteristic peaks were observed at 529.8 and 531.6 eV, attributed to the Ti–O and hydroxyl species, respectively.

For investigating the photocatalytic performance of $TiO_{2-H}$ and M–$TiO_2$ (M = Au, Ag, Pt, and Pd) composites toward the oxidation of aromatic alcohols, selective oxidation of benzyl alcohol was utilized as a probe reaction [27,54,55]. First, the oxidation of benzyl alcohol was investigated without catalysts under visible-light irradiation. In this case, benzaldehyde was barely formed (not shown). Next, the reaction was performed by adding 10 mg of the catalyst under 1 atm $O_2$. The solution temperature was rigorously maintained at 30 °C using a water-cooling system. Fig. 7 summarizes the amounts of benzaldehyde formed after 4 h of reaction conducted under visible-light irradiation (Xe lamp, 300 W, λ > 460 nm). Notably, benzaldehyde was selectively obtained in the presence of the catalyst. In the dark, the oxidation of benzyl alcohol did not occur with the use of pristine $TiO_2$ ($TiO_{2-H}$), whereas 9.13% benzyl alcohol was oxidized under visible-light irradiation; this visible-light-driven activity is attributed to the ligand-to-metal charge transfer (LMCT) of the surface complex formed by the adsorption of benzyl alcohol on the $TiO_2$ surface [56–58]. Subsequently, effective improvement in the photocatalytic performance was observed for M–$TiO_2$ (M = Au, Ag, Pt, and Pd) composites as compared to $TiO_{2-H}$. Among all the samples, $Pt_2$–$TiO_2$ nanocomposite exhibited the best visible-light photoactivity towards the selective oxidation of benzyl alcohol and is almost 10 times as high as that of $TiO_{2-H}$. In contrast, the photocatalytic activity of $Pd_2$–$TiO_2$ was four times as high as that of $TiO_{2-H}$, whereas $Au_2$–$TiO_2$ and $Ag_2$–$TiO_2$ only exhibited 3 and 2 times higher activity, respectively. Meanwhile, the selectivity of M–$TiO_2$ for the selective oxidation of benzyl alcohol under visible-light irradiation (>95%) was significantly greater than that for $TiO_{2-H}$, corresponding to only 73.8%, as shown in Fig. 7(b). Moreover, the photocatalytic activity of M–$TiO_2$ (M = Au, Ag, Pt, and Pd) composites depends on the amount of the loaded noble metal. As shown in Fig. 7(a), the yield of benzaldehyde increased with the loading of noble metals; this increased visible-light photoactivity is attributed to the greater light absorbance for the high loading amount of metal and is consistent with the absorption cross sections in Fig. S4. As reported, the rate-determining step of the oxidation of benzyl alcohol over M–$TiO_2$ is the injection of hot electrons into the semiconductor CB. In this case, the increasing visible-light absorbance of M–$TiO_2$ (M = Au, Ag, Pt, and Pd) could provide additional energy to the electrons to overcome the Schottky barrier and facilitate the transfer of electrons to the semiconductor CB, thus enhancing the yield.

For better understanding the enhancement of photocatalytic performance over M–$TiO_2$ (M = Au, Ag, Pt, and Pd) catalysts, the effects of light wavelength on photocatalytic activity were investigated. Specific optical filter glasses (filter 1: 490 nm–800 nm, filter 2: 560 nm–800 nm, and filter 3: 620 nm–800 nm) were used for blocking light below cut-off wavelengths, as shown in Fig. 8(a). As the reaction temperature was maintained at 30 °C, the thermal effect contribution remained unchanged. In this case, the thermal effect contribution at room temperature (30 °C) over M–$TiO_2$ (M = Au, Ag, Pt, and Pd) of all the photocatalysts was negligible (Fig. 9 (b–e)). Hence, the contribution of light at different wavelength ranges can be estimated from the results acquired by irradiation using cut-off filters. When light with wavelengths in the full 460 nm to 800 nm range irradiated at the reaction system of $Pt_2$-$TiO_2$ system, a reaction yield of 86% was obtained. Applying a filter that blocked wavelengths below 490 nm, the obtained decrease in the yield of 31.74% (=86.12%–54.38%), which accounts for 36.85% of the overall yield achieved. From the results obtained from the tuning irradiation wavelength, we can estimate the contribution of the light in a narrow wavelength range. As shown by the results in Fig. 8, light irradiation at wavelengths ranging from 490 nm to 620 nm resulted in the highest enhancement in yield, for the Au- and Ag-loaded photocatalysts, accounting for 76.72% and 70.7% of the total light irradiation enhancement, respectively. As for Pt- and Pd-loaded photocatalysts, the main contribution of light was observed in the wavelength ranges 460–560 nm (77.76% and 80.45%). Given that the main absorbance peaks of Au and Ag NPs are in the wavelength range between 490 and 620 nm, and Pt

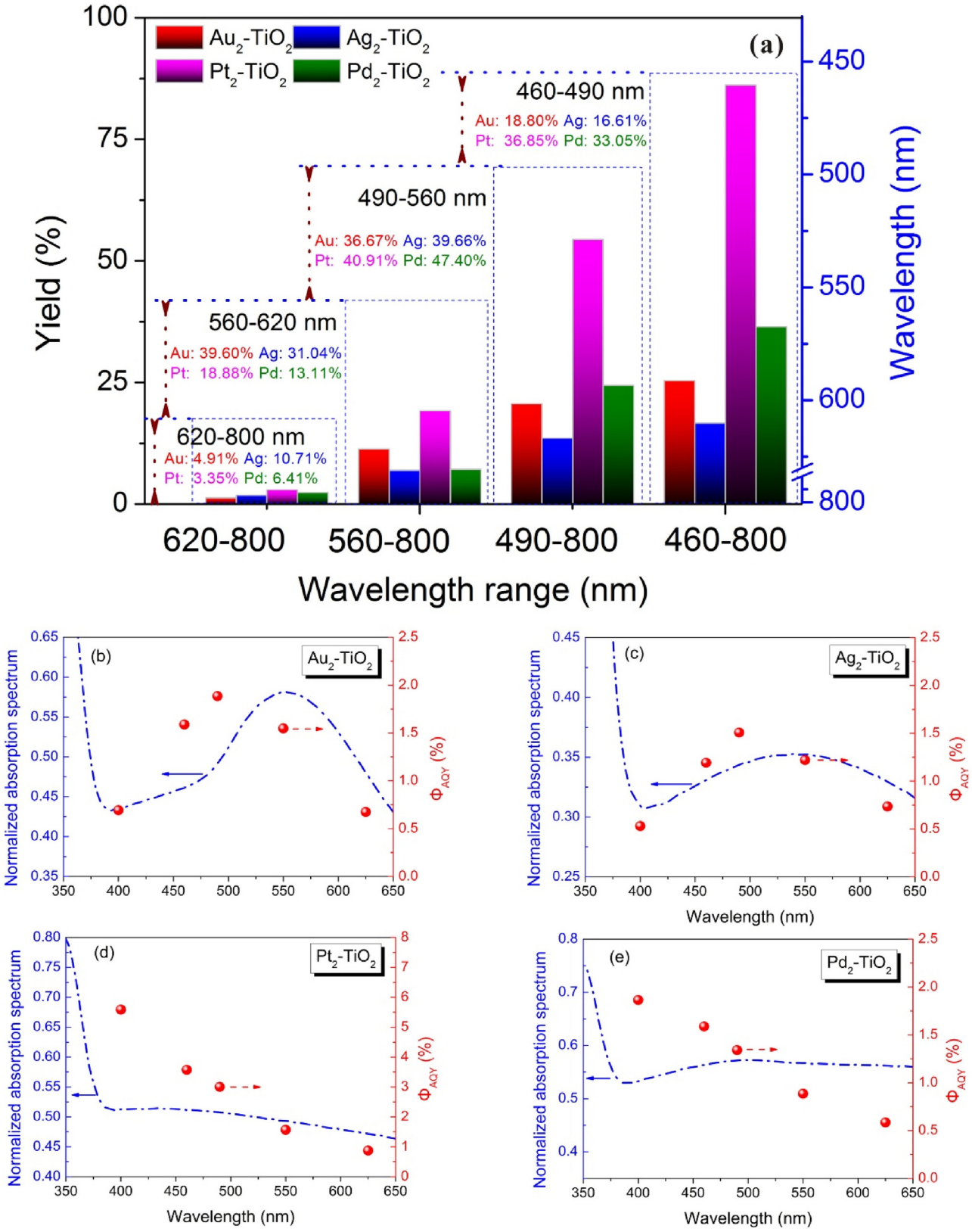


**Fig. 8.** (a) Dependence of yield and irradiation wavelength over 2 wt% M–$TiO_2$ (M = Au, Ag, Pt, and Pd) catalysts for the selective oxidation of benzyl alcohol. Both the light-driven reaction and the reaction in the dark were conducted at 30 °C. (b, c, d, and e) Diffuse-reflectance UV–vis spectra of 2 wt% M–$TiO_2$ (M = Au, Ag, Pt, and Pd) catalysts and the quantum yield for the formation of benzaldehyde under an LED lamp irradiation of different wavelengths such as purple, blue, green, yellow, and red light. The apparent quantum yield was calculated using the equation $\Phi_{AQY} = (Y_{vis} - Y_{dark})/N \times 100\%$, where $Y_{vis}$ and $Y_{dark}$ denote the yield of benzaldehyde under light and dark conditions, respectively. *N* denotes the number of incident photons in the reaction vessel.

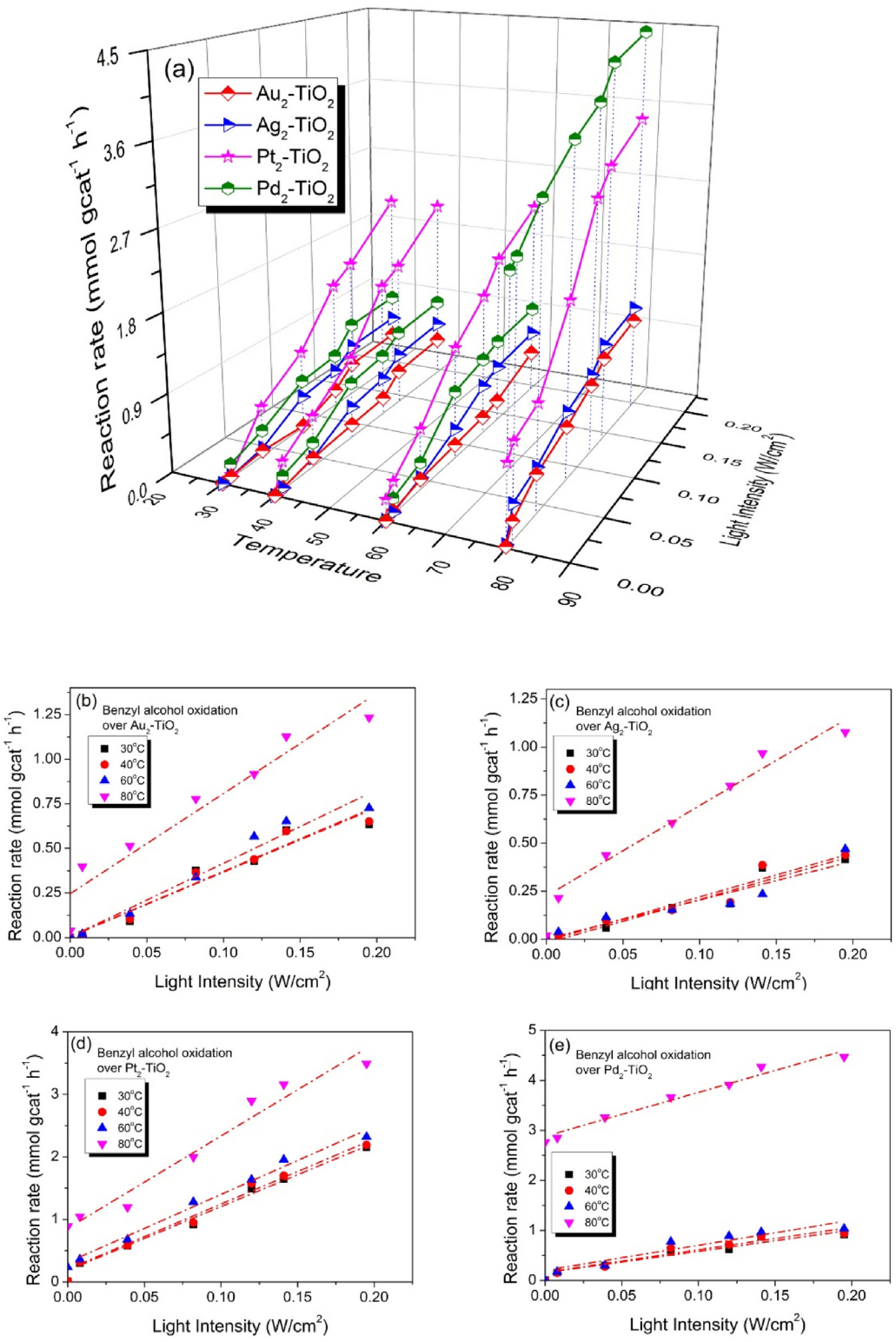


**Fig. 9.** (a) Dependence of the photocatalytic activity of 2 wt% M–$TiO_2$ (M = Au, Ag, Pt, and Pd) catalysts for the oxidation of benzyl alcohol on light intensity and operating temperature. (b, c, d, and e) Rate of photocatalytic reaction over 2 wt% M–$TiO_2$ as a function of irradiance intensity at various temperatures (M = Au, Ag, Pt, and Pd) catalysts.

and Pd NPs are in the range of 460–560 nm. It is suggested that the visible-light absorption of noble metal plays an important role in enhancing the photo-reaction yield. In addition, the above experiments show that the irradiation wavelength parameters of the light source are very important in photochemical reactions.

The effect of irradiation wavelength on the catalytic reaction rate was also confirmed by irradiation using monochromatic light LEDs. When the reactor was irradiated at different wavelength lights, such as purple (395–400 nm), blue (465–470 nm), yellow (485–490 nm), green (525–530 nm), and red (625–630 nm) with the other experimental conditions maintained constant, the trend of quantum yield was similar to that observed in the absorption spectrum. Fig. 8(b–e) shows the plots of the rate of the photocatalytic reaction versus wavelength of light irradiation. The action

spectra indicate that the dependence of the apparent quantum yield (AQY%) of the reactions catalyzed by the supported photocatalysts on the irradiation wavelength is remarkably similar to the light absorption spectra. This data clearly suggests that the enhancement of the aerobic oxidation over M–$TiO_2$ catalysts is triggered by the activation of metal particles. Notably, the $Pt_2$–$TiO_2$ catalyst exhibited the highest $\Phi_{AQY}$ in a broad wavelength range of incident light, especially at 400 nm < λ < 500 nm, and the $\Phi_{AQY}$ values for the $Pt_2$–$TiO_2$ catalyst at 400 and 460 nm were 5.58% and 3.57%, respectively; these values are significantly greater than that obtained with the $TiO_{2\text{-}H}$ catalyst (Fig. S6). This observation suggests that the electronic excitation of Pt particles by visible light enables the transfer of electrons to $TiO_2$ and promotes the reduction of $O_2$. According to a previous investigation [59], platinum clusters are strongly adsorbed onto the anatase surface via association with steps, terraces, and oxygen vacancy sites, and the adsorption energy of Pt/anatase is 10 times greater than that of Au/anatase. Therefore, it can be speculated that the strong affinity between Pt nanoparticles and the anatase $TiO_2$ is beneficial to the transformation of $e^-$ at the Pt–$TiO_2$ interface, thereby accumulating these transferred electrons in the $TiO_2$ CB [35]. Furthermore, metal deposition strongly attenuated the migration of photo-excited carriers, the photoluminescence signals indicate that the charge-separation efficiency follows the order: $Pt_2$–$TiO_2$ > $Pd_2$–$TiO_2$ > $Au_2$–$TiO_2$ > $Ag_2$–$TiO_2$ > $TiO_{2\text{-}H}$. Therefore, it is suggested that the noble metal may function as an electron acceptor ("electron sink"), thereby increasing the number of charge carriers available [60].

As previously reported by Sarina et al., operating temperature and light intensity are critical to the photocatalytic performance for the oxidation of benzyl alcohol [61]. For understanding the effect of these two factors for photocatalytic processing, the oxidation of benzyl alcohol using six attenuation slices was conducted at four ambient temperatures (30, 40, 60, and 80 °C), and these slices were plotted against the reaction rate. As shown in Fig. 9(a), operating temperature and light intensity were related to the photocatalytic reaction rate, particularly at attaining a temperature of 80 °C. Upon further analysis (Figs. 9(b–e) and S7), the linear dependence of photo-enhancement on light irradiance for all the photocatalysts demonstrated that photoexcitation is a factor primarily responsible for light-enhanced activity. With respect to the operating temperature, at a temperature of less than 60 °C, the thermal effect on the photoreaction can be ignored; in contrast, when the operating temperature reached 80 °C, a significant increase in the photocatalytic reaction rate was observed. $Pd_2$–$TiO_2$ exhibited the highest thermal activity, where the reaction rate was approximately five times as high as that at 30 °C. In contrast, the most photoactive catalyst $Pt_2$–$TiO_2$ also exhibited 1.6 times improvement. Notably,

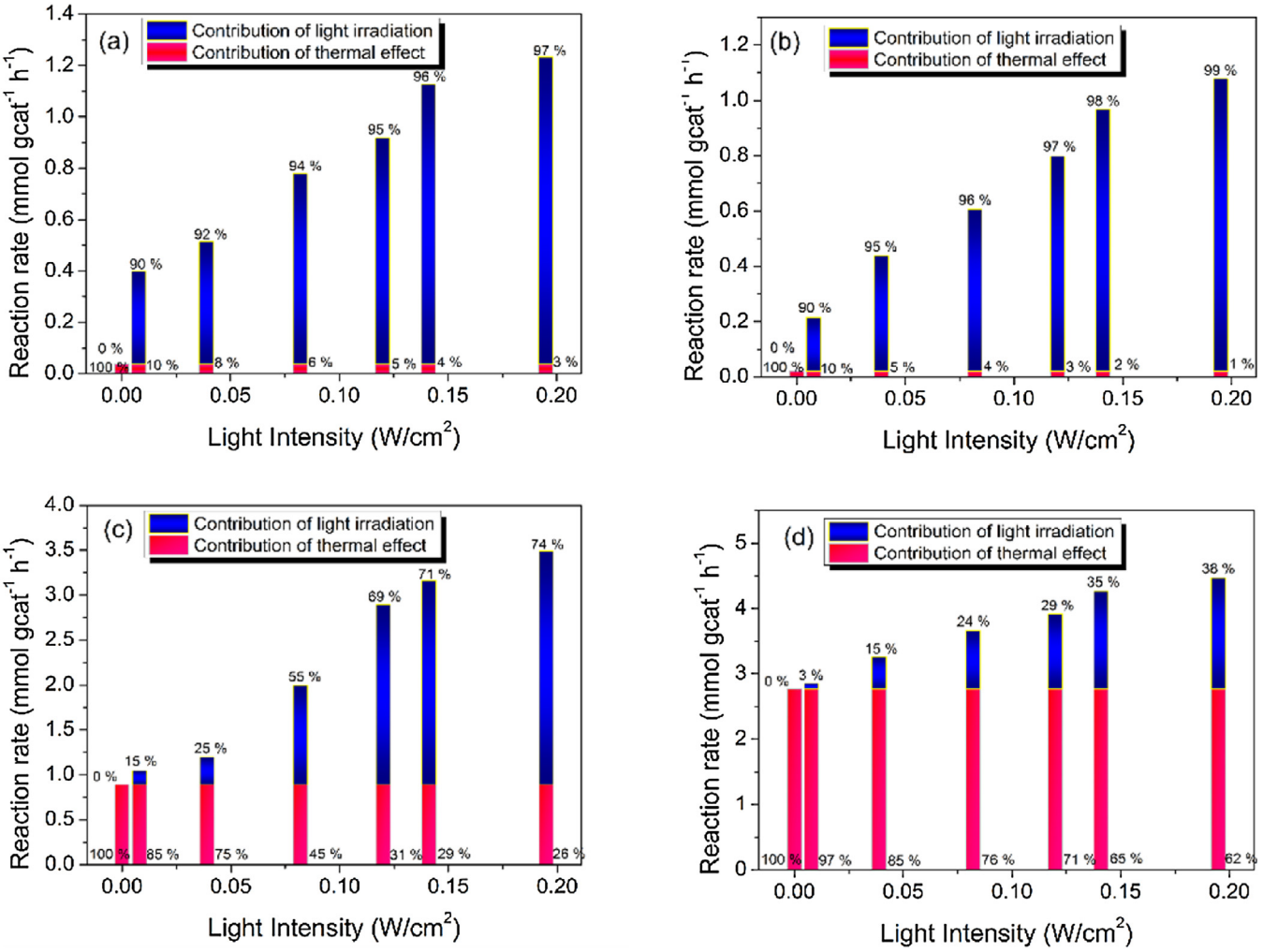


**Fig. 10.** Dependence of the contributions from light irradiation and the thermal effect on the light intensity for oxidation of benzyl alcohol to benzaldehyde over (a) $Au_2$–$TiO_2$, (b) $Ag_2$–$TiO_2$, (c) $Pt_2$–$TiO_2$, and (d) $Pd_2$–$TiO_2$ at 80 °C. The temperature of the reaction was maintained at 80 °C, when the irradiance was changed. The contribution due to light irradiation to the reaction rate was calculated by subtracting the rate of the reaction in the dark (performed at the same temperature) from the rate under light irradiation. The relative contributions of light irradiation and thermal catalysis to the reaction rate could then be determined.

both $Pt_2$–$TiO_2$ and $Pd_2$–$TiO_2$ photocatalysts exhibited high reaction activity at an operating temperature of 80 °C, especially at a high illumination intensity (0.195 W/cm$^2$), and the reaction rates were 4.47 and 3.49 mmol gcat$^{-1}$ h$^{-1}$. Despite the promotion of thermal catalytic efficiency for the gold and silver nanoparticles was not significant as that exhibited by palladium, 1.9 and 2.6 times than that at 30 °C, respectively, the reaction rates still reached 1.23 and 1.07 mmol gcat$^{-1}$ h$^{-1}$, respectively. As shown in Fig. 10, the dependence of the contributions from light irradiation and thermal effect was calculated. The temperature of the reaction was maintained at 80 °C when the irradiation changed, and the relative contributions of light irradiation and thermal catalysis to the reaction rate could be determined. It was found that the contribution of the thermal effect of $Pt_2$-$TiO_2$ was 85% at low illumination, and the higher light intensities result in a larger light enhanced contribution to the total reaction rate. Compared to the $Pt_2$-$TiO_2$, the $Pd_2$-$TiO_2$ is dominated by the thermal effect even at a high illumination (62%). Accordingly, temperature exerted a two-fold effect on the rate of the photocatalytic reaction. First, high temperature results in a great quantity of the adsorbed reactant molecules with the excited states based on the Bose–Einstein distribution, indicating that the reactant molecules (benzyl alcohol) can overcome the activation barrier by using less energy. Second, noble metal nanoparticles possibly produce high-energy-level electrons at high temperature and can be excited by light irradiation, affording more electrons with sufficient energy to induce reactions with the benzyl alcohol molecules adsorbed on the metal NPs. Hence, the ability of platinum and palladium nanoparticles to utilize thermal energy also leads to the use of infrared radiation, an important component of sunlight, to promote the chemical reactions [15,29].

In order to determine the role of photogenerated electrons transfer process under light illumination, the photoelectrochemical characterizations were further authenticated. The I–t curves corresponding to visible-light turning on and off measured at zero bias voltage are presented in Fig. 11(a). Notably, compared to the pristine $TiO_{2\text{-}H}$, the $Pt_2$–$TiO_2$ composite significantly enhances the photocurrent density. The obvious increase in the transient photocurrent was mainly due to two aspects: (i) The Pt NPs present can absorb visible light and generate more photoelectrons because of the intraband or interband transition. (ii) The formation of an Schottky junction at the Pt-$TiO_2$ interface can separate the photoelectrons and holes, and thus increase the photocurrent. Subsequently electrochemical impedance spectroscopy (EIS) was utilized to investigate the electron generation and the charge transport characteristics of $Pt_2$–$TiO_2$ and $TiO_{2\text{-}H}$. As shown in Fig. 11(b), the $Pt_2$–$TiO_2$ sample shows a smaller semicircle in the middle-frequency region, in comparison to the $TiO_{2\text{-}H}$. The smaller arc radius of the EIS plot corresponds to more effective separation of the photoinduced electron–hole and the faster interfacial charger transfer to the electron donor [62]. Owing to the fact that the absorption of visible-light by Pt nanoparticles and the excellent electron transport properties hinder the fast recombination of photoelectron and hole pairs, such composite photocatalyst are largely beneficial for improving visible light photoactivity towards the aerobic oxidation of alcohols.

Herein, the underlying reaction mechanism involved for the photocatalytic oxidation of benzyl alcohol over $Pt_2$–$TiO_2$ catalyst was investigated by conducting controlled experiments. Previous studies have clarified that molecular oxygen is the oxidizing agent for several photo-driven reactions catalyzed by $TiO_2$, and the most critical part is the adsorption of molecular oxygen on the $TiO_2$ surface during photocatalysis oxidation process. For better understanding this process, a series of radical scavengers were used in controlled experiments for probing the reaction mechanism for the selective oxidation of benzyl alcohol over $Pt_2$–$TiO_2$ under visible-light irradiation. As shown in Fig. 12, in Ar atmosphere, the conversion of benzyl alcohol can be ignored, as only 6.2% conversion was observed; however, under air, a higher conversion was observed (80.5%), but this conversion was still less than that observed in pure oxygen (86.1%). This phenomenon indicates that oxygen is an essential oxidant substance in the photocatalytic reaction process. Moreover, when TBA was used as a radical scav-

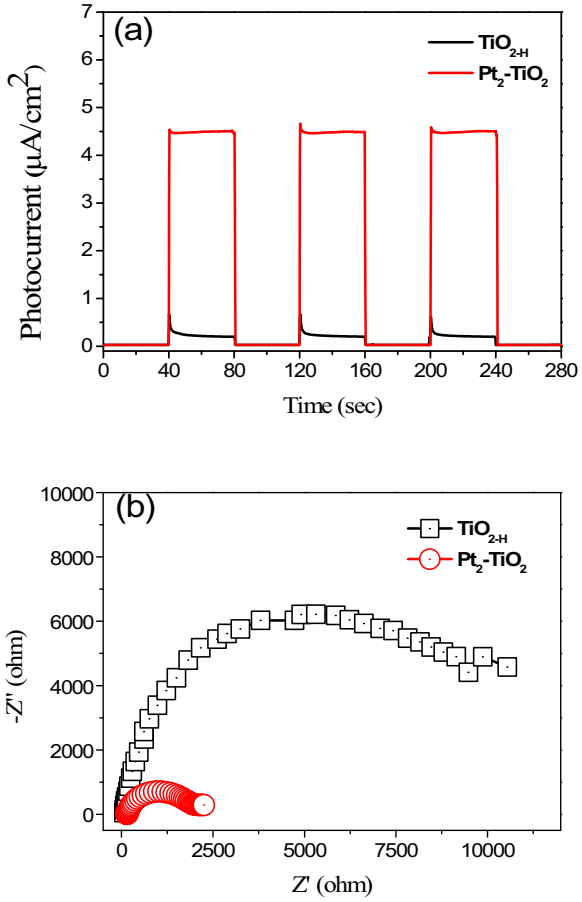


**Fig. 11.** Photocurrent transient response (a) and electrochemical impedance spectroscopy Nyquist plots (b) of the sample electrodes of $Pt_2$-$TiO_2$ and $TiO_{2\text{-}H}$ under visible light irradiation.

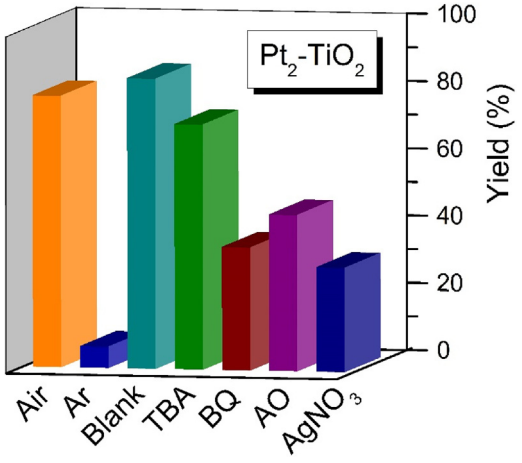


**Fig. 12.** Controlled experiments using different radical scavengers (a) $AgNO_3$ for photogenerated electrons, (b) *p*-benzoquinone (BQ) for superoxide radicals; (c) AO for photogenerated holes; (d) *tert*-butyl alcohol (TBA) for hydroxyl radicals; (e) absence of radical scavengers for the selective photocatalytic oxidation of benzyl alcohol over $Pt_2$–$TiO_2$. Reaction conducted under Ar (f) and under air (g).

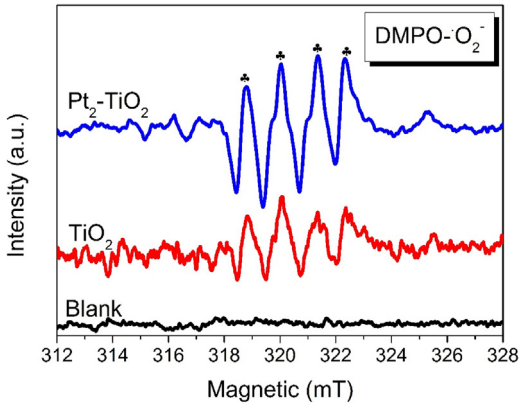


**Fig. 13.** ESR spectra of the radical adduct trapped by DMPO (DMPO-·$O^{2-}$) over the $TiO_{2\text{-}H}$ and $Pt_2$-$TiO_2$ nanocomposites in a 40 mM DMPO methanol solution under visible-light irradiation. All the spectra were recorded after 5 min of visible-light irradiation. Blank represents the sample containing the spin probe alone under light illumination.

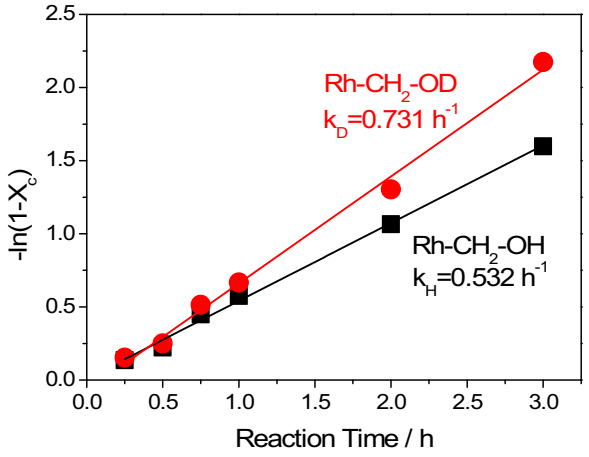


**Fig. 14.** Comparison between the photo-oxidation of Rh-$CH_2$-OH and Rh-$CH_2$-OD. The slopes of the lines, $k_H$ and $k_D$, stand for the rate constants of the reactions with benzyl alcohol and deuterium-benzyl alcohol, respectively.

enger for •OH radicals, no significant change in the reaction process was observed. However, yield abruptly decreased with the addition of ammonium oxalate, $AgNO_3$, and benzoquinone for capturing the photogenerated holes ($h^+$), photoelectrons ($e^-$), and superoxide radicals (•$O^{2-}$), respectively. The observed results indicate that either the photogenerated holes and electrons or superoxide radicals are involved in the photocatalytic reaction over $Pt_2$–$TiO_2$ under visible-light irradiation, and •OH radicals are not the primary reactive species for benzyl alcohol oxidation. In addition, it is well known that the •OH radical is a highly reactive oxygen species, which could indiscriminately oxidize benzyl alcohol molecules with no selectivity. In contrast, the superoxide species is a known oxidant for selective oxidation of alcohols. Therefore, the superoxide species with mild oxidative behaviors and the absence of hydroxyl radicals in this system could favorably react with benzyl alcohol and might be the major reason for the high selectivity. Based on the above controlled experimental results, it can be deduced that molecular oxygen possibly serves to trap photogenerated electrons, affording surperoxide radicals, which could inhibit the recombination of photogenerated charge carriers and facilitate the selective oxidation of benzyl alcohol. For identifying the reactive species and further understanding the mechanism for the enhancement of the photocatalytic performance of $Pt_2$–$TiO_2$, ESR technique using specific spin trapping agent was carried out in the reaction process. Herein, 5,5-dimethyl-1-pyrroline-N-oxide (DMPO) was selected as a spin trap agent for superoxide radicals [63,64]. Fig. 13 shows the ESR spectra recorded from the solutions containing DMPO spin probe of $TiO_2$ or $Pt_2$–$TiO_2$ during visible-light irradiation. As shown in Fig. 13, upon irradiation for 5 min in the presence of $TiO_2$ or $Pt_2$–$TiO_2$, a spectrum characteristic for the DMPO-•$O^{2-}$ adduct was observed. Besides, the intensity of the radical signal for $Pt_2$–$TiO_2$ was stronger than that of $TiO_2$, suggesting that superoxide radicals were generated over the pristine $TiO_2$, confirming that •$O^{2-}$ radicals are indeed produced on $Pt_2$–$TiO_2$ during the reaction and play a decisive role in the photocatalytic oxidation of benzyl alcohol.

For considering the rate-determining step, the kinetic solvent isotope effect of the as-prepared $Pt_2$-$TiO_2$ was conducted with benzyl alcohol under aerobic conditions. Herein, we choose the deuterated benzyl alcohol (Rh-$CH_2$-OD, 98% CDN ISOTOPES INC.) by replacing the hydrogen of oxhydryl with deuterium. Rh-$CH_2$-OD was oxidized under the same conditions as the reaction of Rh-$CH_2$-OH over $Pt_2$-$TiO_2$. The conversion of benzyl alcohol ($X_C$) was calculated, and a first-order dependence of the reaction rate on the concentration of benzyl alcohol was found. The plot of $-\ln(1-X_C)$ versus the reaction time $t$ creates several straight lines according to the equation of first-order reaction: $-\ln(1-X_C) = kt$, in which $k$ is the rate constant of the reaction. To describe the change quantitatively, the kinetic isotope effect is expressed as the ratio of the rate constants of the reactions involving the light ($k_H$) and the heavy ($k_D$) isotopically substituted reactants: KIE = $k_H/k_D$. In general, the hydrogen kinetic isotope effect can be classified into primary hydrogen kinetic isotope effect (PHKIE) and secondary hydrogen kinetic isotope effect (SHKIE). The PHKIE refers to cases in which a bond to the isotopically labeled hydrogen is formed or broken, whereas the SHKIE arises in cases where the isotopic substitution is remote from the bond being broken. Typically, the kinetic isotope effect (KIE) of PHKIE is located between 2 and 7, whereas SHKIE is between 0.7 and 1.5 [65–67]. From the simulations (Fig. 14), the slope of the line corresponds to the rate constant $k$: $k_H = 0.532\ h^{-1}$ for Rh-$CH_2$-OH and $k_D = 0.731\ h^{-1}$ for Rh-$CH_2$-OD. Thus, the KIE is determined to be 0.727, suggesting that the KIE of such reaction belongs to SHKIE. The result indicates that the bond breakage of —$CH_2$– is the rate-determining step of the overall reaction.

Considering the above results, a plausible mechanism for the photocatalytic oxidation of benzyl alcohol over Pt–$TiO_2$ was proposed, as illustrated in Fig. 15. Once platinum nanoparticles and $TiO_2$ contacted, an Schottky barrier ($\Phi_{SB}$) was formed at the interface between platinum and $TiO_2$, with the CB and valence band bending upward to the $TiO_2$ interface [26,35,68,69]. Visible-light irradiation resulted in the collective oscillation of the sp band or d band electrons on the metal nanoparticles, which in turn promote intra- or interband excitation to the CB. Then, the *hot electrons* with energies sufficiently high to overcome the Schottky barrier are injected into the CB of the neighboring $TiO_2$. The *hot electrons* on the $TiO_2$ surface can be scavenged by molecular oxygen molecules, yielding active superoxide radical species [70,71]. These superoxide species abstract the α-H atoms from the cleavage of C–H bond on the methylene group (–$CH_2$–) of benzyl alcohol to form an alkoxide intermediate and is considered to be the rate-determining step. Subsequently, the transient alkoxide intermediate undergoes a rapid hydride shift, resulting in the elimination of protonic hydrogen and affording the product. The possible mechanism provides a reasonable explanation for the photo-oxidation of alcohols over Pt–$TiO_2$ photocatalyst under visible-light irradiation.

Inspired by the efficient photoactivity of $Pt_2$–$TiO_2$ for the selective oxidation of benzyl alcohol, the photocatalytic oxidation of other aromatic alcohols over $Pt_2$–$TiO_2$ and $TiO_{2\text{-}H}$ was tested, as listed in Table 2. As expected, $Pt_2$–$TiO_2$ has the highest photocatalytic activity for the oxidation of aromatic alcohol

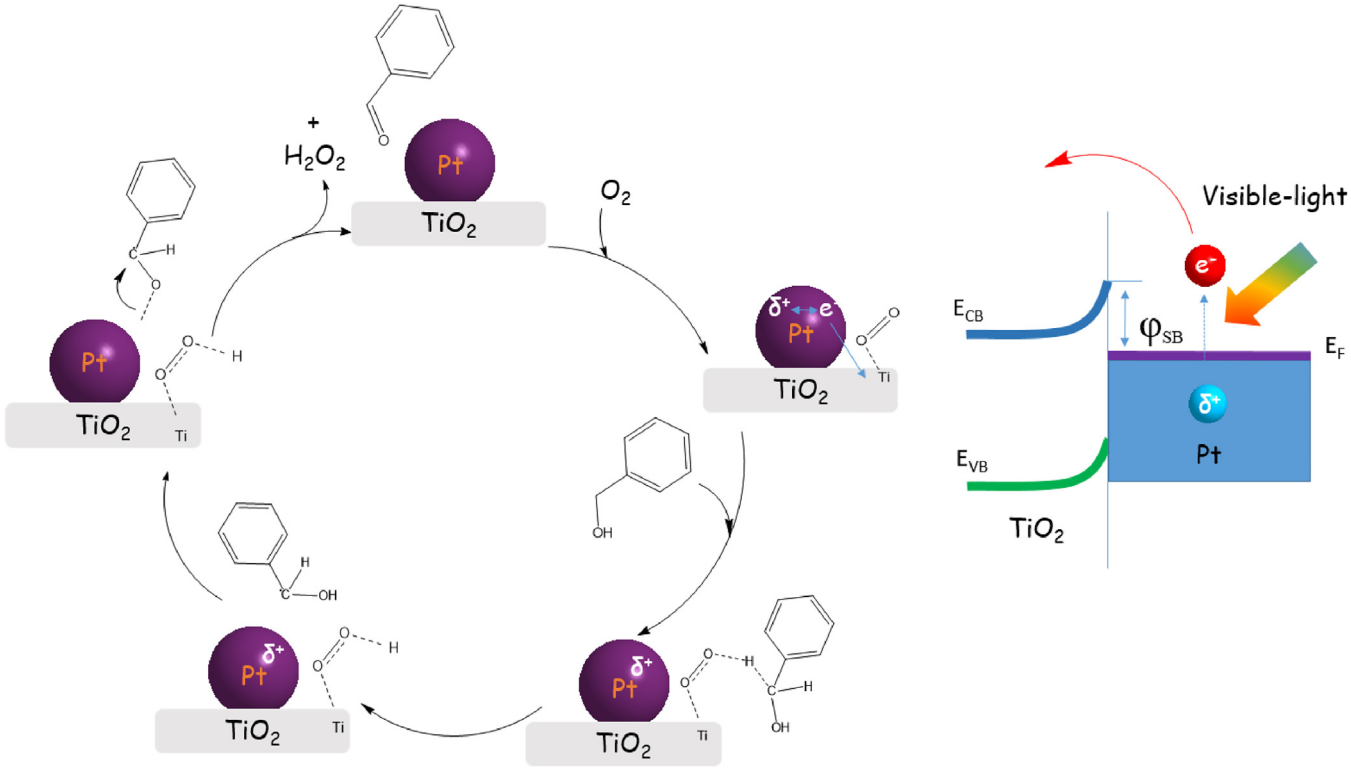


**Fig. 15.** Proposed reaction mechanism for the production of benzaldehyde over Pt-$TiO_2$ under visible-light irradiation. $E_F$, $E_{CB}$, and $E_{VB}$ were assigned to the Fermi level, conduction band and valence band for Pt, and support material $TiO_2$.

and is several times higher than the reference $TiO_{2\text{-}H}$. Also, the reaction exhibited good selectivity to carbonyl compounds. Furthermore, there were significant differences in the yield of different aromatic aldehydes or ketones. The formation rate of *para*-substituted benzaldehyde over $Pt_2$–$TiO_2$ decreased in the following order: 4–methoxybenzyl alcohol > 4–methylbenzyl alcohol > benzyl alcohol > 4–chlorobenzyl alcohol and is consistent with the electron-releasing effect of the substituted group. As explained by the Hammett rule, the substitution of *para*-substituted benzylic alcohols with electron-releasing groups such as —$OCH_3$ and —$CH_3$ could improve the efficiency of the reaction in contrast to the substitution with —Cl decreasing the activity [57]. The above results suggested that the $Pt_2$–$TiO_2$ composite is an excellent photocatalyst for the selective oxidation of aromatic alcohols to the corresponding carbonyl compounds.

At last, the $Pt_2$–$TiO_2$ nanocomposite also exhibited good reusability of the photocatalytic oxidation of benzyl alcohol. The structure of the catalyst remained unchanged (Fig. S8) after the reaction, indicating excellent stability. The recycle reaction results (Fig. S9) illustrate no obvious change in the yield after the 5th reaction cycle. The yields of 83.31%, 81.96%, and 78.33% were obtained in the second, third, and fourth reaction cycles, respectively. For the fifth reaction cycle, a conversion of greater than 74.15% was still achieved.

## 4. Conclusions

In conclusion, noble-metal nanoparticles (Au, Ag, Pt, and Pd) were successively deposited on the $TiO_2$ nanocrystal with hollow structures by photodeposition. As compared to the pristine $TiO_{2\text{-}H}$, the resulting M–$TiO_2$ (M = Au, Ag, Pt, and Pd) nanocomposites exhibited enhanced photoactivity towards the selective oxidation of benzyl alcohol under visible-light irradiation. The enhanced photoactivity is predominantly attributed to the contribution from noble-metal nanoparticles in increasing visible-light absorbance and creating a Schottky barrier at the heterojunction, which in turn provide additional energetic photo-electrons and facilitate the transferring of electrons from metal to anatase. Meanwhile, direct correlation was observed between the light intensity, light wavelength, reaction temperature, and photocatalytic activity of prepared photocatalysts, suggesting that the rate of alcohol oxidation is enhanced by increasing the illumination intensity or reaction temperature or by adjusting irradiation wavelength to the most suitable range. In particular, $Pt_2$–$TiO_2$, (~2 nm) when supported on $TiO_2$ behaves as an efficient visible-light-driven catalyst for aerobic oxidation at room temperature. The visible-light absorption of Pt nanoparticles produces a large number of *hot electrons* via the interband transition of their 5d electrons and crosses over the Schottky barrier at the interface between the metal and semiconductor and activates $O_2$, as well as produces a large number of surperoxide species, which behave as key active species for oxidation. The $Pt_2$–$TiO_2$ catalysts promote the aerobic oxidation of alcohols with an apparent quantum yield of 5.58% (400 nm), which is almost 14 times as high as that exhibited by the $TiO_{2\text{-}H}$ catalyst (0.4%). The investigation of the KIE for the oxidation of benzyl alcohol suggested the breaking the C–H bond of benzyl alcohol as the rate determining step. The reaction mechanism of the photocatalytic reaction over $Pt_2$–$TiO_2$ is proposed by using different radical scavengers and ESR analysis. Finally, the results obtained by changing reaction temperature indicated that platinum and palladium NPs also effectively couple thermal and light energy sources to more efficiently drive chemical transformation.

## Acknowledgements

This study was supported by International Joint Research Projects in the Science & Technology Pillar Program of Tianjin, China (13RCGFSF14300), Research Projects in the Science & Technol-

**Table 2**
Aerobic oxidation of aromatic alcohols over $TiO_{2-H}$ and the $Pt_2$–$TiO_2$ photocatalysts[a].

| Entry | Substrate | Product | Catalyst | Yield [b](%) | Selectivity [c](%) | Reaction rate (mmol $gcat^{-1}$ $h^{-1}$) |
|---|---|---|---|---|---|---|
| 1 | 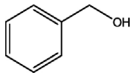 | 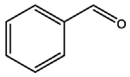 | $Pt_2$–$TiO_2$ | 99 | >99 | 1.663 |
| | | | $TiO_{2-H}$ | 23.7 | 74.2 | 0.532 |
| 2 | 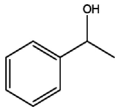 | 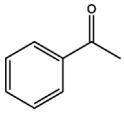 | $Pt_2$–$TiO_2$ | 95.1 | 99.1 | 1.599 |
| | | | $TiO_{2-H}$ | 14.6 | 76.2 | 0.319 |
| 3[d] | 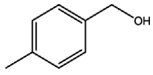 | 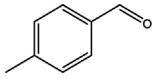 | $Pt_2$–$TiO_2$ | 99.2 | >99 | 3.330 |
| | | | $TiO_{2-H}$ | 37.7 | 76.8 | 1.636 |
| 4 | 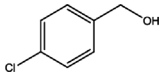 | 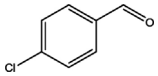 | $Pt_2$–$TiO_2$ | 97.6 | 98.4 | 1.653 |
| | | | $TiO_{2-H}$ | 17.6 | 71.2 | 0.412 |
| 5[e] | 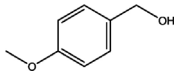 | 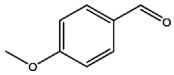 | $Pt_2$–$TiO_2$ | 99.2 | >99 | 3.326 |
| | | | $TiO_{2-H}$ | 30.3 | 74.2 | 1.361 |
| 6 | 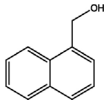 | 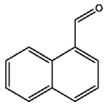 | $Pt_2$–$TiO_2$ | 80.6 | 90.1 | 1.491 |
| | | | $TiO_{2-H}$ | 12.8 | 63.8 | 0.334 |
| 7 | 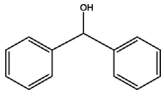 | 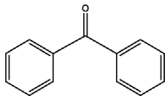 | $Pt_2$–$TiO_2$ | 78.1 | 85.8 | 1.517 |
| | | | $TiO_{2-H}$ | 10.8 | 64.2 | 0.280 |

[a] Reaction conditions: trifluorotoluene (1.5 mL), alcohol (0.1 mmol), catalyst (10 mg), $O_2$ (1 atm), reaction temperature 30 °C, Reaction time 6 h, illumination Source: 20 W white LED lamp.
[b] Aromatic aldehyde yield.
[c] selective of aldehyde or ketone.
[d] Reaction time 3 h.
[e] Reaction time 3 h.

ogy Pillar Program of Tianjin, China (14TXGCCX00012), Research Projects in the Science & Technology Pillar Program of Tianjin, China (15JCTPJC63300), Research Projects in the Science & Technology Program of Jinnan District Tianjin, China (2015JNKW0005) and the Ph.D. Candidate Research Innovation Fund of Nankai University.

## Appendix A. Supplementary data

Supplementary data associated with this article can be found, in the online version, at http://dx.doi.org/10.1016/j.apcatb.2017.03.077.

## References

[1] A. Abad, P. Concepción, A. Corma, H. García, A collaborative effect between gold and a support induces the selective oxidation of alcohols, Angew. Chem. Int. Ed. 44 (2005) 4066–4069.
[2] D.I. Enache, J.K. Edwards, P. Landon, B. Solsona-Espriu, A.F. Carley, A.A. Herzing, M. Watanabe, C.J. Kiely, D.W. Knight, G.J. Hutchings, Solvent-free oxidation of primary alcohols to aldehydes using Au-Pd/TiO2 catalyst, Science 311 (2006) 362–365.
[3] G.L. Brett, Q. He, C. Hammond, P.J. Miedziak, N. Dimitratos, M. Sankar, A.A. Herzing, M. Conte, J.A. Lopez-Sanchez, C.J. Kiely, D.W. Knight, S.H. Taylor, G.J. Hutchings, Selective oxidation of glycerol by highly active bimetallic catalysts at ambient temperature under base-free conditions, Angew. Chem. – Int. Ed. 50 (2011) 10136–10139.
[4] G.J. Ten Brink, I.W.C.E. Arends, R.A. Sheldon, Green, catalytic oxidation of alcohols in water, Science 287 (2000) 1636–1639.
[5] T. Mallat, A. Baiker, Oxidation of alcohols with molecular oxygen on solid catalysts, Chem. Rev. 104 (2004) 3037–3058.
[6] C. Parmeggiani, F. Cardona, Transition metal based catalysts in the aerobic oxidation of alcohols, Green Chem. 14 (2012) 547–564.
[7] S.E. Davis, M.S. Ide, R.J. Davis, Selective oxidation of alcohols and aldehydes over supported metal nanoparticles, Green Chem. 15 (2013) 17–45.
[8] F.M. Menger, C. Lee, Synthetically useful oxidations at solid sodium permanganate surfaces, Tetrahedron Lett. 22 (1981) 1655–1656.
[9] M. Zhang, C. Chen, W. Ma, J. Zhao, Visible-light-induced aerobic oxidation of alcohols in a coupled photocatalytic system of dye-sensitized $TiO_2$ and TEMPO, Angew. Chem. Int. Ed. 47 (2008) 9730–9733.
[10] V. Augugliaro, G. Camera-Roda, V. Loddo, G. Palmisano, L. Palmisano, J. Soria, S. Yurdakal, Heterogeneous photocatalysis and photoelectrocatalysis: from unselective abatement of noxious species to selective production of high-value chemicals, J. Phys. Chem. Lett. 6 (2015) 1968–1981.
[11] J.C. Colmenares, R. Luque, Heterogeneous photocatalytic nanomaterials: prospects and challenges in selective transformations of biomass-derived compounds, Chem. Soc. Rev. 43 (2014) 765–778.
[12] N. Zhang, Y. Zhang, X. Pan, X. Fu, S. Liu, Y.J. Xu, Assembly of CdS nanoparticles on the two-dimensional graphene scaffold as visible-light-driven photocatalyst for selective organic transformation under ambient conditions, J. Phys. Chem. C 115 (2011) 23501–23511.
[13] S. Yurdakal, G. Palmisano, V. Loddo, V. Augugliaro, L. Palmisano, Nanostructured rutile TiO2 for selective photocatalytic oxidation of aromatic alcohols to aldehydes in water, J. Am. Chem. Soc. 130 (2008) 1568–1569.
[14] M. Zhang, Q. Wang, C. Chen, L. Zang, W. Ma, J. Zhao, Oxygen atom transfer in the photocatalytic oxidation of alcohols by $TiO_2$: Oxygen isotope studies, Angew. Chem. Int. Ed. 48 (2009) 6081–6084.
[15] S. Sarina, H. Zhu, E. Jaatinen, Q. Xiao, H. Liu, J. Jia, C. Chen, J. Zhao, Enhancing catalytic performance of palladium in gold and palladium alloy nanoparticles for organic synthesis reactions through visible light irradiation at ambient temperatures, J. Am. Chem. Soc. 135 (2013) 5793–5801.

[16] Y. Chen, W. Li, J. Wang, Y. Gan, L. Liu, M. Ju, Microwave-assisted ionic liquid synthesis of $Ti^{3+}$ self-doped $TiO_2$ hollow nanocrystals with enhanced visible-light photoactivity, Appl. Catal. B: Environ. 191 (2016) 94–105.
[17] X. Pan, Y.J. Xu, Efficient thermal- and photocatalyst of Pd nanoparticles on $TiO_2$ achieved by an oxygen vacancies promoted synthesis strategy, ACS Appl. Mater. Interfaces 6 (2014) 1879–1886.
[18] X. Dai, M. Xie, S. Meng, X. Fu, S. Chen, Coupled systems for selective oxidation of aromatic alcohols to aldehydes and reduction of nitrobenzene into aniline using CdS/g-$C_3N_4$ photocatalyst under visible light irradiation, Appl. Catal. B Environ. 158–159 (2014) 382–390.
[19] J.A. Terrett, J.D. Cuthbertson, V.W. Shurtleff, D.W.C. MacMillan, Switching on elusive organometallic mechanisms with photoredox catalysis, Nature 524 (2015) 330–334.
[20] Q. Xiao, Z. Liu, A. Bo, S. Zavahir, S. Sarina, S. Bottle, J.D. Riches, H. Zhu, Catalytic transformation of aliphatic alcohols to corresponding esters in o2 under neutral conditions using visible-light irradiation, J. Am. Chem. Soc. 137 (2015) 1956–1966.
[21] Y. Liu, P. Zhang, B. Tian, J. Zhang, Core-shell structural CdS@$SnO_2$ nanorods with excellent visible-light photocatalytic activity for the selective oxidation of benzyl alcohol to benzaldehyde, ACS Appl. Mater Interfaces 7 (2015) 13849–13858.
[22] X. Lang, W. Ma, C. Chen, H. Ji, J. Zhao, Selective aerobic oxidation mediated by $TiO_2$ photocatalysis, Acc. Chem. Res. 47 (2014) 355–363.
[23] D.S. Ovoshchnikov, B.G. Donoeva, V.B. Golovko, Visible-light-driven aerobic oxidation of amines to nitriles over hydrous ruthenium oxide supported on $TiO_2$, ACS Catal. 5 (2015) 34–38.
[24] H. Sakamoto, T. Ohara, N. Yasumoto, Y. Shiraishi, S. Ichikawa, S. Tanaka, T. Hirai, Hot-electron-induced highly efficient $O_2$ activation by Pt nanoparticles supported on $Ta_2O_5$ driven by visible light, J. Am. Chem. Soc. 137 (2015) 9324–9332.
[25] Y. Shiraishi, H. Sakamoto, Y. Sugano, S. Ichikawa, T. Hirai, Pt-Cu bimetallic alloy nanoparticles supported on anatase $TiO_2$: Highly active catalysts for aerobic oxidation driven by visible light, ACS Nano 7 (2013) 9287–9297.
[26] D. Tsukamoto, Y. Shiraishi, Y. Sugano, S. Ichikawa, S. Tanaka, T. Hirai, Gold nanoparticles located at the interface of anatase/rutile $TiO_2$ particles as active plasmonic photocatalysts for aerobic oxidation, J. Am. Chem. Soc. 134 (2012) 6309–6315.
[27] Y. Sugano, Y. Shiraishi, D. Tsukamoto, S. Ichikawa, S. Tanaka, T. Hirai, Supported Au-Cu bimetallic alloy nanoparticles: an aerobic oxidation catalyst with regenerable activity by visible-light irradiation, Angew. Chem. Int. Ed. 52 (2013) 5295–5299.
[28] F. Wang, Z. Lu, L. Yang, Y. Zhang, Q. Tang, Y. Guo, X. Ma, Z. Yang, Palladium nanoparticles with high energy facets as a key factor in dissociating $O_2$ in the solvent-free selective oxidation of alcohols, Chem. Commun. 49 (2013) 6626–6628.
[29] S. Sarina, H.Y. Zhu, Q. Xiao, E. Jaatinen, J. Jia, Y. Huang, Z. Zheng, H. Wu, Viable photocatalysts under solar-spectrum irradiation: nonplasmonic metal nanoparticles, Angew. Chem. – Int. Ed. 53 (2014) 2935–2940.
[30] Z.H.N. Al-Azri, W.T. Chen, A. Chan, V. Jovic, T. Ina, H. Idriss, G.I.N. Waterhouse, The roles of metal co-catalysts and reaction media in photocatalytic hydrogen production: performance evaluation of M/$TiO_2$ photocatalysts (M = Pd, Pt, Au) in different alcohol-water mixtures, J. Catal. 329 (2015) 355–367.
[31] P. Zhang, T.D. Wang, J. Gong, Mechanistic understanding of the plasmonic enhancement for solar water splitting, Adv. Mater. 27 (2015) 5328–5342.
[32] A. Li, P. Zhang, X. Chang, W. Cai, T. Wang, J. Gong, Gold nanorod@$TiO_2$ yolk-shell nanostructures for visible-light-driven photocatalytic oxidation of benzyl alcohol, Small 11 (2015) 1892–1899.
[33] A. Tanaka, S. Sakaguchi, K. Hashimoto, H. Kominami, Preparation of Au/$TiO_2$ with metal cocatalysts exhibiting strong surface plasmon resonance effective for photoinduced hydrogen formation under irradiation of visible light, ACS Catal. 3 (2013) 79–85.
[34] A. Tanaka, K. Hashimoto, H. Kominami, Preparation of Au/$CeO_2$ exhibiting strong surface plasmon resonance effective for selective or chemoselective oxidation of alcohols to aldehydes or ketones in aqueous suspensions under irradiation by green light, J. Am. Chem. Soc. 134 (2012) 14526–14533.
[35] Y. Shiraishi, D. Tsukamoto, Y. Sugano, A. Shiro, S. Ichikawa, S. Tanaka, T. Hirai, Platinum nanoparticles supported on anatase titanium dioxide as highly active catalysts for aerobic oxidation under visible light irradiation, ACS Catal. 2 (2012) 1984–1992.
[36] Z. Zheng, B. Huang, X. Qin, X. Zhang, Y. Dai, M.H. Whangbo, Facile in situ synthesis of visible-light plasmonic photocatalysts M@$TiO_2$ (M = Au, Pt Ag) and evaluation of their photocatalytic oxidation of benzene to phenol, J. Mater. Chem. 21 (2011) 9079–9087.
[37] S. Sarina, E.R. Waclawik, H. Zhu, Photocatalysis on supported gold and silver nanoparticles under ultraviolet and visible light irradiation, Green Chem. 15 (2013) 1814–1833.
[38] J. Wang, B. Li, T. Gu, T. Ming, J. Wang, P. Wang, J.C. Yu, (Gold core) at (ceria shell) nanostructures for plasmon-enhanced catalytic reactions under visible light, ACS Nano 8 (2014) 8152–8162.
[39] J. Wang, P. Rao, W. An, J. Xu, Y. Men, Boosting photocatalytic activity of Pd decorated $TiO_2$ nanocrystal with exposed (001) facets for selective alcohol oxidations, Appl. Catal. B: Environ. 195 (2016) 141–148.
[40] M. Diak, E. Grabowska, A. Zaleska, Synthesis, characterization and photocatalytic activity of noble metal-modified $TiO_2$ nanosheets with exposed {001} facets, Appl. Surf. Sci. 347 (2015) 275–285.
[41] L. Liu, T.D. Dao, R. Kodiyath, Q. Kang, H. Abe, T. Nagao, J. Ye, Plasmonic janus-composite photocatalyst comprising Au and C-$TiO_2$ for enhanced aerobic oxidation over a broad visible-light range, Adv. Funct. Mater. 24 (2014) 7754–7762.
[42] M. Murdoch, G.I.N. Waterhouse, M.A. Nadeem, J.B. Metson, M.A. Keane, R.F. Howe, J. Llorca, H. Idriss, The effect of gold loading and particle size on photocatalytic hydrogen production from ethanol over Au/$TiO_2$ nanoparticles, Nat. Chem. 3 (2011) 489–492.
[43] A. Wood, M. Giersig, P. Mulvaney, Fermi level equilibration in quantum dot-metal nanojunctions, J. Phys. Chem. B 105 (2001) 8810–8815.
[44] P. Mulvaney, Surface plasmon spectroscopy of nanosized metal particles, Langmuir 12 (1996) 788–800.
[45] X. Pan, Y.J. Xu, Defect-mediated growth of noble-metal (Ag, Pt, and Pd) nanoparticles on $TiO_2$ with oxygen vacancies for photocatalytic redox reactions under visible light, J. Phys. Chem. C 117 (2013) 17996–18005.
[46] D. Jiang, W. Wang, S. Sun, L. Zhang, Y. Zheng, Equilibrating the plasmonic and catalytic roles of metallic nanostructures in photocatalytic oxidation over Au-modified $CeO_2$, ACS Catal. 5 (2015) 613–621.
[47] D. Lu, S. Ouyang, H. Xu, D. Li, X. Zhang, Y. Li, J. Ye, Designing Au surface-modified nanoporous-single-crystalline $SrTiO_3$ to optimize diffusion of surface plasmon resonance-induce photoelectron toward enhanced visible-light photoactivity, ACS Appl. Mater. Interfaces 8 (2016) 9506–9513.
[48] V. Jovic, Z.H.N. Al-Azri, W.T. Chen, D. Sun-Waterhouse, H. Idriss, G.I.N. Waterhouse, Photocatalytic $H_2$ production from ethanol-water mixtures over Pt/$TiO_2$ and Au/$TiO_2$ photocatalysts: a comparative study, Top. Catal. 56 (2013) 1139–1151.
[49] N. Serpone, D. Lawless, R. Khairutdinov, Size effects on the photophysical properties of colloidal anatase $TiO_2$ particles: size quantization or direct transitions in this indirect semiconductor? J. Phys. Chem. 99 (1995) 16646–16654.
[50] D. Ding, K. Liu, S. He, C. Gao, Y. Yin, Ligand-exchange assisted formation of Au/$TiO_2$ Schottky contact for visible-light photocatalysis, Nano Lett. 14 (2014) 6731–6736.
[51] S. Zhu, S. Liang, Q. Gu, L. Xie, J. Wang, Z. Ding, P. Liu, Effect of Au supported $TiO_2$ with dominant exposed {001} facets on the visible-light photocatalytic activity, Appl. Catal. B Environ. 119–120 (2012) 146–155.
[52] N. Kruse, S. Chenakin, XPS characterization of Au/$TiO_2$ catalysts: binding energy assessment and irradiation effects, Appl. Catal. A Gen. 391 (2011) 367–376.
[53] C. Liu, Q. Kuang, Z. Xie, L. Zheng, The effect of noble metal (Au, Pd and Pt) nanoparticles on the gas sensing performance of $SnO_2$-based sensors: a case study on the {221} high-index faceted $SnO_2$ octahedra, CrystEngComm 17 (2015) 6308–6313.
[54] S. Verma, R.B.N. Baig, M.N. Nadagouda, R.S. Varma, Selective oxidation of alcohols using photoactive VO@g-$C_3N_4$, ACS Sustainable Chem. Eng. 4 (2016) 1094–1098.
[55] T. Jiang, C. Jia, L. Zhang, S. He, Y. Sang, H. Li, Y. Li, X. Xu, H. Liu, Gold and gold-palladium alloy nanoparticles on heterostructured $TiO_2$ nanobelts as plasmonic photocatalysts for benzyl alcohol oxidation, Nanoscale 7 (2015) 209–217.
[56] S. Higashimoto, N. Kitao, N. Yoshida, T. Sakura, M. Azuma, H. Ohue, Y. Sakata, Selective photocatalytic oxidation of benzyl alcohol and its derivatives into corresponding aldehydes by molecular oxygen on titanium dioxide under visible light irradiation, J. Catal. 266 (2009) 279–285.
[57] S. Higashimoto, N. Suetsugu, M. Azuma, H. Ohue, Y. Sakata, Efficient and selective oxidation of benzylic alcohol by $O_2$ into corresponding aldehydes on a $TiO_2$ photocatalyst under visible light irradiation: effect of phenyl-ring substitution on the photocatalytic activity, J. Catal. 274 (2010) 76–83.
[58] H. Kobayashi, S. Higashimoto, DFT study on the reaction mechanisms behind the catalytic oxidation of benzyl alcohol into benzaldehyde by $O_2$ over anatase $TiO_2$ surfaces with hydroxyl groups: role of visible-light irradiation, Appl. Catal. B: Environ. 170–171 (2015) 135–143.
[59] X.Q. Gong, A. Selloni, O. Dulub, P. Jacobson, U. Diebold, Small Au and Pt clusters at the anatase TiO2(101) surface: behavior at terraces, steps, and surface oxygen vacancies, J. Am. Chem. Soc. 130 (2008) 370–381.
[60] A. Bumajdad, M. Madkour, Understanding the superior photocatalytic activity of noble metals modified titania under UV and visible light irradiation, Phys. Chem. Chem. Phys. 16 (2014) 7146–7158.
[61] S. Sarina, S. Bai, Y. Huang, C. Chen, J. Jia, E. Jaatinen, G.A. Ayoko, Z. Bao, H. Zhu, Visible light enhanced oxidant free dehydrogenation of aromatic alcohols using Au-Pd alloy nanoparticle catalysts, Green Chem. 16 (2014) 331–341.
[62] Y. Zhang, N. Zhang, Z.-R. Tang, Y.-J. Xu, A unique silk mat-like structured Pd/$CeO_2$as an efficient visible light photocatalyst for green organic transformation in water, ACS Sustainable Chem. Eng. 1 (2013) 1258–1266.
[63] J. Yang, X. Wang, Y. Chen, J. Dai, S. Sun, Enhanced photocatalytic activities of visible-light driven green synthesis in water and environmental remediation on Au/$Bi_2WO_6$ hybrid nanostructures, RSC Adv. 5 (2015) 9771–9782.
[64] H. Fu, L. Zhang, S. Zhang, Y. Zhu, J. Zhao, Electron spin resonance spin-trapping detection of radical intermediates in N-doped $TiO_2$-assisted photodegradation of 4-chlorophenol, J. Phys. Chem. B 110 (2006) 3061–3065.
[65] S. Higashimoto, K. Okada, M. Azuma, H. Ohue, T. Terai, Y. Sakata, Characteristics of the charge transfer surface complex on titanium(iv) dioxide for the visible light induced chemo-selective oxidation of benzyl alcohol, RSC Adv. 2 (2012) 669–676.
[66] A. Li, T. Wang, X. Chang, W. Cai, P. Zhang, J. Zhang, J. Gong, Spatial separation of oxidation and reduction co-catalysts for efficient charge separation:

pt@$TiO_2$@MnOxhollow spheres for photocatalytic reactions, Chem. Sci. 7 (2016) 890–895.
[67] X. Zhang, X. Ke, Z. Zheng, H. Liu, H. Zhu, $TiO_2$ nanofibers of different crystal phases for transesterification of alcohols with dimethyl carbonate, Appl. Catal. B: Environ. 150–151 (2014) 330–337.
[68] C. Clavero, Plasmon-induced hot-electron generation at nanoparticle/metal-oxide interfaces for photovoltaic and photocatalytic devices, Nat. Photonics 8 (2014) 95–103.
[69] M.R. Khan, T.W. Chuan, A. Yousuf, M.N.K. Chowdhury, C.K. Cheng, Schottky barrier and surface plasmonic resonance phenomena towards the photocatalytic reaction: study of their mechanisms to enhance photocatalytic activity, Catal. Sci. Technol. 5 (2015) 2522–2531.
[70] P. Christopher, H. Xin, A. Marimuthu, S. Linic, Singular characteristics and unique chemical bond activation mechanisms of photocatalytic reactions on plasmonic nanostructures, Nat. Mater. 11 (2012) 1044–1050.
[71] P. Christopher, H. Xin, S. Linic, Visible-light-enhanced catalytic oxidation reactions on plasmonic silver nanostructures, Nat. Chem. 3 (2011) 467–472.